FLUID DYNAMICS OF CAVITATING SONIC TWO-PHASE FLOW IN A CONVERGING-DIVERGING NOZZLE

by

WILLIAM ASHER

B.S., Kansas State University, 2008

A THESIS

submitted in partial fulfillment of the requirements for the degree

MASTER OF SCIENCE

Department of Mechanical and Nuclear Engineering
College of Engineering

KANSAS STATE UNIVERSITY
Manhattan, Kansas

2014

Approved by:

Major Professor
Steven Eckels

Copyright

Abstract

Both cavitating and flashing flows are important phenomena in fluid flow. Cavitating flow, a common consideration in valves, orifices, and metering devices, is also a concern in loss of coolant accidents for liquid water in power plants when saturation pressures are below atmospheric pressure. Flashing flow is a common consideration for devices such as relief and expansion valves and fluid injectors as well as for loss of coolant accidents in which the coolant's saturation pressure is above atmospheric. Of the two phenomena, flashing flow has received greater interest due to its applicability to safety concerns, though cavitating flow is perhaps of greater interest in terms of energy efficiency.

It is possible for cavitating and flashing flow to actually become sonic. That is, the local velocity of a fluid can exceed the local speed of sound due to the unique properties of two-phase mixtures. When a flow becomes sonic, it is possible for the flow to accelerate and impose additional energy losses that would not otherwise occur. Models of this aspect of two-phase flow are not well developed, typically only being presented for the case of constant area ducts.

In this paper two models for cavitating sonic flow are developed and described by applying the integral forms of the mass, momentum, and energy equations to a control volume of variable cross-sectional area. These models, based on the homogeneous equilibrium model (HEM) and separated flow model, are then applied to experimental data taken by the author with R-134a as the fluid of interest. Experimental data were taken with four instrumented converging-diverging nozzles of various geometries using a custom testing rig that allowed for precise control and measurement of flow parameters such as mass flow, temperature, and pressure. The resultant data from the models are then examined, focusing on the resultant velocities, Mach numbers, quality, and shear stresses.

Table of Contents

List of Figures

List of Tables

Acknowledgements

I would like to thank my family and friends for understanding why I wished to continue with my education and for helping me achieve that goal. I would like to thank the members of my committee and the faculty and staff of the KSU MNE Department for their patience, understanding, and help, especially when it comes to deadlines. I would also like to thank the people and staff of the IER and my former coworkers at Caitin for their help in achieving this research. I would especially like to thank Dr. Eckels for his upbeat attitude, certainty that this degree would get done, and patience with my "vacation" in California. Thank you all for making this possible.

Preface

The research shown in this report was carried out in cooperation with the startup company Caitin (formerly New Pax) investigating a new thermodynamic refrigeration cycle. The cycle consists of pumping the working fluid as a liquid into a converging-diverging nozzle. The fluid then absorbs heat due to the phase change caused by the pressure dropping below saturation pressure, with the pressure drop being due to the acceleration of the flow as it becomes sonic. Further down the nozzle, the flow shocks back to a liquid at a higher temperature than when it entered. Heat rejection then takes place before the flow enters the pump to begin the cycle over again. The main novelty in this cycle is that work on the fluid is performed by a pump on a liquid as opposed to a compressor on a gas, having potential to be more efficient. Another possible benefit was thought to be the potential of water as a refrigerant with the new cycle, compared with the volume problems that water vapor poses with vapor-compression systems.

Research performed by the author and others at Kansas State University proved that the cycle exists as described, but the lack of cycle efficiency compared with traditional refrigeration cycles, such as vapor-compression or absorption, limit commercial applications. However, the detailed data taken in researching the cycle has provided for a large amount of possibility in the analysis and understanding of two-phase flow. The research described in this paper deals only with an adiabatic flow, neglecting any heat transfer, though data involving heat transfer was collected.

Nomenclature

Abbreviations

HEM	Homogeneous Equilibrium Model
IFM	Inlet flow modifier
NIST	National Institute of Standards and Technology
PID	Proportional integral derivative
VFD	Variable frequency drive
VI	Virtual instrument

Greek Symbols

α	Void fraction
θ	Angle
ρ	Density
τ	Shear stress

Mathematical Symbols

A	Cross-sectional area
A^*	Throat cross-sectional area
c	Speed of sound
d	Diameter
F	Force
F_τ	Force on wall due to shear
g	Acceleration of gravity
H	Head loss
h	Specific enthalpy
h_{lv}	Specific latent heat of vaporization
$\vec{k}$	Unit vector of z-direction
L	Length
M	Mach number
Ma	Total mass
$\dot{m}$	Mass flow rate
n	Exponent in slip ratio S definition
p	Pressure
$\vec{P}$	Linear momentum
$\dot{Q}$	Rate of heat transfer
r	Radius
S	Slip ratio
t	Time
V	Velocity
$\forall$	Volume
$\dot{W}$	Rate of work
x	Quality
z	Location in z-direction, zero at throat

Subscripts

C	Converging section
D	Diverging section
i	i-th pressure tap
l	Liquid phase
max	Maximum
t	Throat
v	Vapor

Chapter 1 - Literature Review

In this paper two models for cavitating sonic flow are developed and described by applying the integral forms of the mass, momentum, and energy equations to a control volume of variable cross-sectional area. These models, based on the homogeneous equilibrium model (HEM) and separated flow model, are then applied to experimental data taken by the author with R-134a as the fluid of interest. Experimental data were taken with several instrumented converging-diverging nozzles of various geometries using a custom testing rig that allowed for precise control and measurement of flow parameters such as mass flow, temperature, and pressure. Resultant data from the models are then examined, focusing on the resultant velocities, Mach numbers, quality, and shear stresses.

1.1 Converging-Diverging Nozzle Flow

Flow through a converging-diverging nozzle is essentially flow through a restriction. The behavior of this flow is dependent on the fluid type (liquid, vapor, two-phase mixture) and conditions of the fluid before the restriction, the geometry both before and after the restriction, and the conditions after the restriction. The type of flow considered in this paper pertains to a subcooled liquid entering such a restriction, though the case of a two-phase flow entering a restriction is also briefly discussed. For the subcooled case, there are primarily two distinctions made in terms of when phase change occurs. If the restriction causes a phase change but the flow eventually exits as a liquid, then the flow is cavitating. However, if the flow continues as either a two-phase mixture or as a vapor, then the flow is flashing.

Both cavitating and flashing flow are important phenomena in fluid flow. For example, cavitating flow, a common consideration in ball valves (Chern, Wang et al. 2007), orifices, and metering devices, is also a concern for loss of coolant accidents with liquid water in power plants when saturation pressures are below atmospheric pressure (Schrock, Starkman et al. 1977). Flashing flow is a common consideration for devices such as relief valves (Schmidt and Egan 2009), expansion valves (Yang and Zhang 2005), and fluid injectors (Wirth and Rossmeissl 2006) as well as for loss of coolant accidents in which the coolant's saturation pressure is above atmospheric pressure (Shin and Jones 1993). Of the two phenomena, flashing flow has received greater interest due to its applicability to safety concerns, though cavitating flow is perhaps of greater interest in terms of energy efficiency.

If the inlet is subcooled, it is useful to apply a simple Bernoulli analysis. Four cases of subcooled inlet flow are illustrated in Figure 1.1.

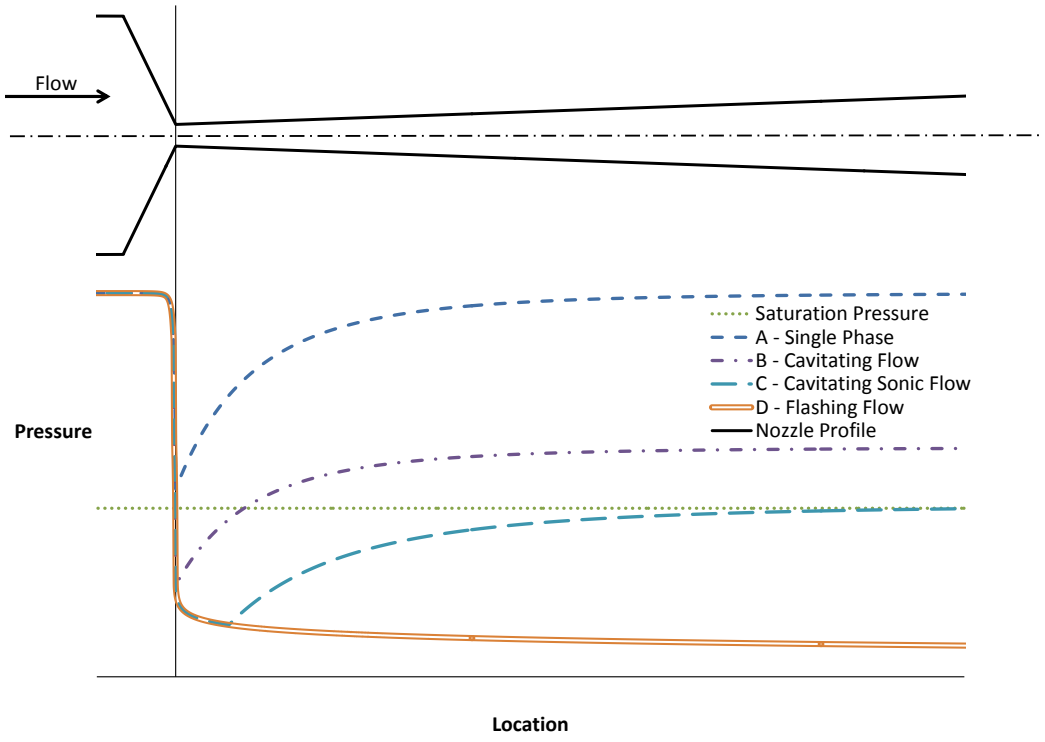

Figure 1.1: Nozzle Pressure Distribution by Flow Type

A line of constant pressure corresponding to the fluid's inlet saturation pressure is drawn across the map. For case A, in which the local pressure does not drop below the saturation pressure as the velocity increases through the throat, the fluid remains a single-phase liquid throughout the nozzle. For cases B, in which the local pressure drops below the saturation pressure then rises back up, the flow is cavitating. At this point, a section of the flow is two-phase, with liquid having changed boiled into vapor. For case C, in which the local pressure drops below the saturation pressure at the throat and continues to decrease, but then rises back to or above the saturation pressure, the flow has accelerated due to sonic conditions and is cavitating. If the pressure rises to above the saturation pressure, then the exit flow is single-phase. If the pressure rises just up to the saturation pressure, the flow may be single-phase or two-phase. For case D, in which the local pressure drops and remains below the saturation pressure at the exit, the flow is flashing.

Part of the difficulty with analyzing liquid flow through a converging-diverging nozzle is that local pressures can drop below the saturation pressure before the throat. This leaves questions as to whether the flow has gone two-phase before or at the throat. In addition, flow structures such as vena contracta can cause a further drop in pressure after the throat, meaning that the flow might not go two-phase until after the throat. Therefore, a subcooled liquid entering a converging-diverging nozzle can go two-phase before, at, or after the throat, or even fail to go two-phase at all. These complications create difficulty when choosing an analysis method.

1.2 Sonic Flow

A flow is considered sonic if the local velocity has reaches or exceededs the local speed of sound. When flow exceeds the speed of sound, it can continue to accelerate even when the

cross-sectional area is expanding. Cases C and D in Figure 1.2 illustrate this acceleration, with decreasing pressure after the physical throat. This is due to the compressible nature of both gas and two-phase flows. Sonic single-phase gas flow through nozzles is a relatively well-understood phenomenon when compared with sonic, two-phase flow through nozzles. Part of the difficulty in analyzing sonic two-phase flow comes from determining the local speed of sound. For single-phase fluids, the speed of sound c is determined by the relationship between pressure and density, described by

$$c^2 = \frac{dp}{d\rho} \qquad [1.1]$$

and is usually evaluated assuming isentropic or isothermal conditions.

For two-phase flows, the flow is often not in either thermodynamic or mechanical equilibrium. In other words, the flow is often not isentropic or isothermal. Therefore, modeling sound speed in two-phase flows becomes more complicated. However if the flow is assumed to be in thermodynamic and mechanical equilibrium, then the sound speeds of each phase, weighted according to void fraction, yield the mixture speed of sound to be (Brennen 1995)

$$c^2 = \left[(\alpha\rho_v + (1-\alpha)\rho_l)\left(\frac{\alpha}{\rho_v c_v^2} + \frac{1-\alpha}{\rho_l c_l^2}\right)\right]^{-1}. \qquad [1.2]$$

Two-phase flow also is unique in that changes in the quality, and thus void fraction, can yield drastically different speeds of sound. The two-phase sound speed for a mixture may be orders of magnitude lower than either the liquid sound speed or vapor sound speed. For example, R-134a at 20°C has liquid and vapor sound speeds of 530 m/s and 145 m/s, respectively. However, the two-phase mixture, as calculated by [1.2], has a sound speed as low as 43 m/s, as illustrated in Figure 1.2.

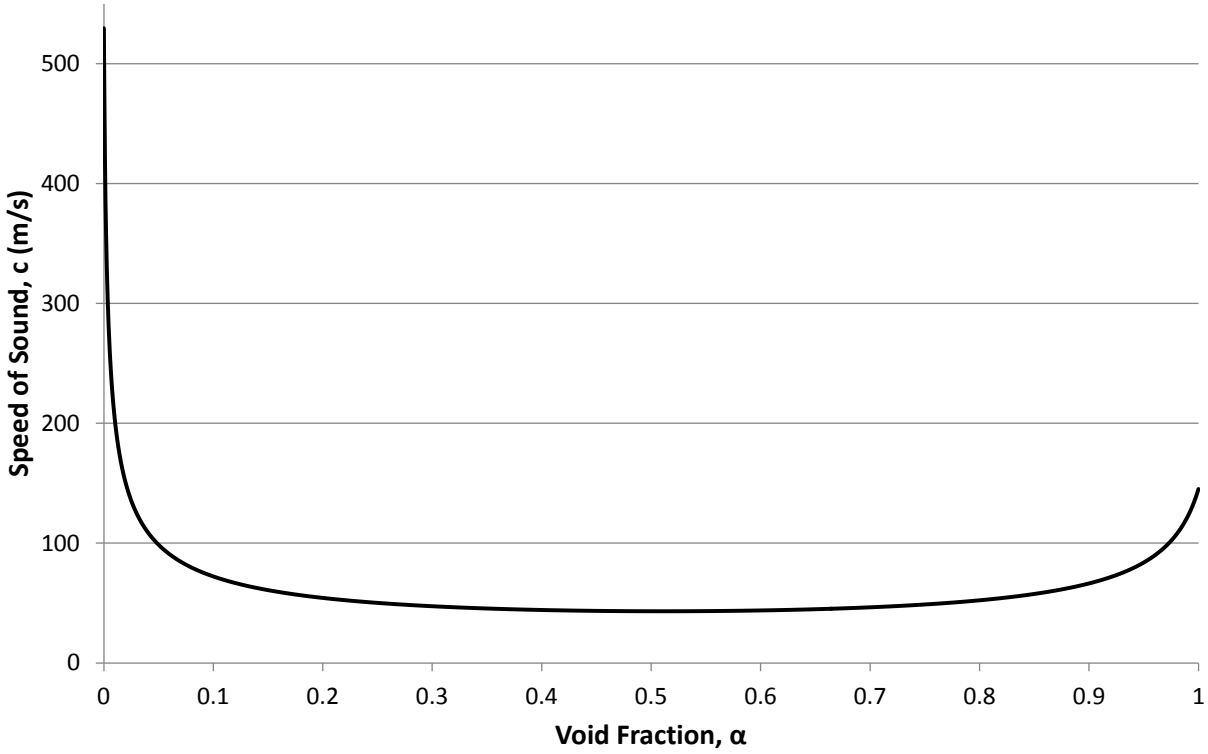

Figure 1.2: Speed of Sound vs. Void Fraction, R-134a at 20°C

Assuming the void fraction, velocity, and single-phase speeds of sound are known for each phase at saturated conditions, [1.2] allows us to find whether a flow is sonic or not by relating the local velocity V to the calculated speed of sound, .i.e. for

$$M = \frac{V}{c} \geq 1 \qquad [1.3]$$

where M is the Mach number. The use of [1.2] is not necessarily valid for all models, but is valid for use with the homogeneous equilibrium model described in Section 1.4.

1.4 Flow Models

There are several basic models that are commonly used to analyze sonic, two-phase flow. Among these are the homogeneous equilibrium model, the separated flow model, and the homogeneous non-equilibrium model. A very comprehensive list of analytical and empirical

models is presented in Elias and Lellouche (1994). Each has distinct strengths and weaknesses related to accuracy, applicability, and ease of calculation. These models are relatively simplistic compared with some models that include bubble dynamics and non-equilibrium phenomena, but are quite useful in being able to describe the basic characteristics of sonic, two-phase flow. For this paper, only the homogeneous equilibrium model and separated flow model are of interest.

Homogeneous Equilibrium Model

The homogeneous equilibrium model, commonly referred to as HEM, is perhaps the most basic of two-phase models. The HEM makes two broad assumptions regarding flow at any given location:

- The phases are in mechanical equilibrium
- The phases are in thermal equilibrium

The first assumption is also referred to as the no-slip condition. Mechanical equilibrium means that the phases are moving without any relative motion to each other. Vapor and liquid can be considered finely dispersed within each other and moving at the same velocity. The lack of relative motion between phases means that interfacial stresses can be ignored. The second assumption of thermal equilibrium means that both phases have identical temperatures and pressures at any given location. Essentially, at any given point the flow is assumed to be at the saturated condition. Variants of this model can include friction, the inclusion of which depends on whether the model is being used to predict or analyze a flow.

Because the HEM makes such broad assumptions, it is usually the least accurate model. However, the HEM is useful as a first-pass model to determine whether or not flow is in the sonic, two-phase region, as it is essentially an ideal case for bubbly flow.

Separated Flow Model

The separated flow model, also known as the non-homogeneous equilibrium model, is similar to the HEM with one exception. It was originally developed by Moody in 1965 as an extension of the HEM that allows for different liquid and vapor velocities. As such, the separated flow model makes the following assumptions regarding flow at any given location:

- The phases are in thermal equilibrium
- The flow has a slip ratio S, defined as the ratio of the vapor velocity to the liquid velocity

The first assumption is the same as for the HEM. Both liquid and vapor have the same temperature and pressure at any given location. The second assumption allows for different liquid and vapor velocities, related to each other by other flow properties. Dependent on the specific application, different variants of the separated flow model have different definitions for the slip ratio S. For this paper, the slip ratio is defined by

$$S = \frac{V_v}{V_l} = \left(\frac{\rho_l}{\rho_v}\right)^n \qquad [1.4]$$

where $n = 1/3$ for Moody's formulation and $n = 1/2$ for Fauske's formulation (Elias and Lellouche 1994). Moody's value is an attempt to theoretically maximize kinetic energy while Fauske's value is based on experimental results. Note that for $n = 0$, $S = 1$ and the separated flow model becomes the HEM.

1.5 Two-Phase Flow Pressure Drop in Constant Area Ducts

A majority of the work in two-phase flow has primarily focused on flow through constant area ducts. This is not unexpected; such flow is common in capillary tubes and heat exchangers. As such, many examples exist of both experimental and theoretical, and such flows are well

understood, at least when compared with two-phase flow in ducts of variable area. Two-phase correlations for pressure drop such as those by Martinelli and others have existed since the 1940s (Wallis 1969). Works such as Yin (1998) and others use two-phase correlations to model pressure drop through capillary tubes. In short, correlations and models exist for two-phase flow pressure drop in constant area ducts.

1.6 Two-Phase Flow Pressure Drop in Variable Area Ducts

Limited experimental work has occurred in the analysis of two-phase pressure drop for cases when the cross-sectional area is not constant. Experimental work that has occurred often neglects certain aspects such as phase change or friction. For example, the works of Ishii, Umeda et al. (1993) or Henry and Fauske (1971) both involved bubbly flow through converging-diverging nozzles, but did not involve phase change or pure liquid up to the throat. The work of Liu, Chen et al. (2008) involved numerically modelling initially subcooled hot water flowing of a converging-diverging nozzle and comparing with the experimental work of Akagawa, Fujii et al. (1987), though this work only dealt with flashing.

1.7 Summary

It has been established that while there is much research on two-phase flow, there is little experimental research for the case of a subcooled liquid cavitating within a converging-diverging nozzle. To that end, the experimental research contained within this paper provides a new set of data and the models developed validate the type of flow occurring. Chapter 2 describes our testing system and the nozzles tested. Chapter 3 contains the development of the models necessary to characterize our data. Chapter 4 discusses and describes the experimental data

without analysis and Chapter 5 describes how the models developed were applied to the data. Finally, Chapter 6 discusses the results of applying the models to experimental data.

Chapter 2 - System Description

The experimental system used for this work is comprised of five main sections consisting of the test section, the refrigerant loop, and three water loops. The test section contains the nozzle and the piping directly upstream and downstream of the nozzle. The refrigerant loop contains the test section and interfaces with the water loops via heat exchangers to provide control over temperatures and pressures. The water loops have equipment and instrumentation to set the temperature of the flowing water.

2.1 Test Section

The test section consists, between the inlet and outlet valves, of a section of inlet piping, a converging-diverging nozzle, and a rapid expansion chamber. The location of the test section is shown in Figure 2.1 in a diagram of the refrigerant loop.

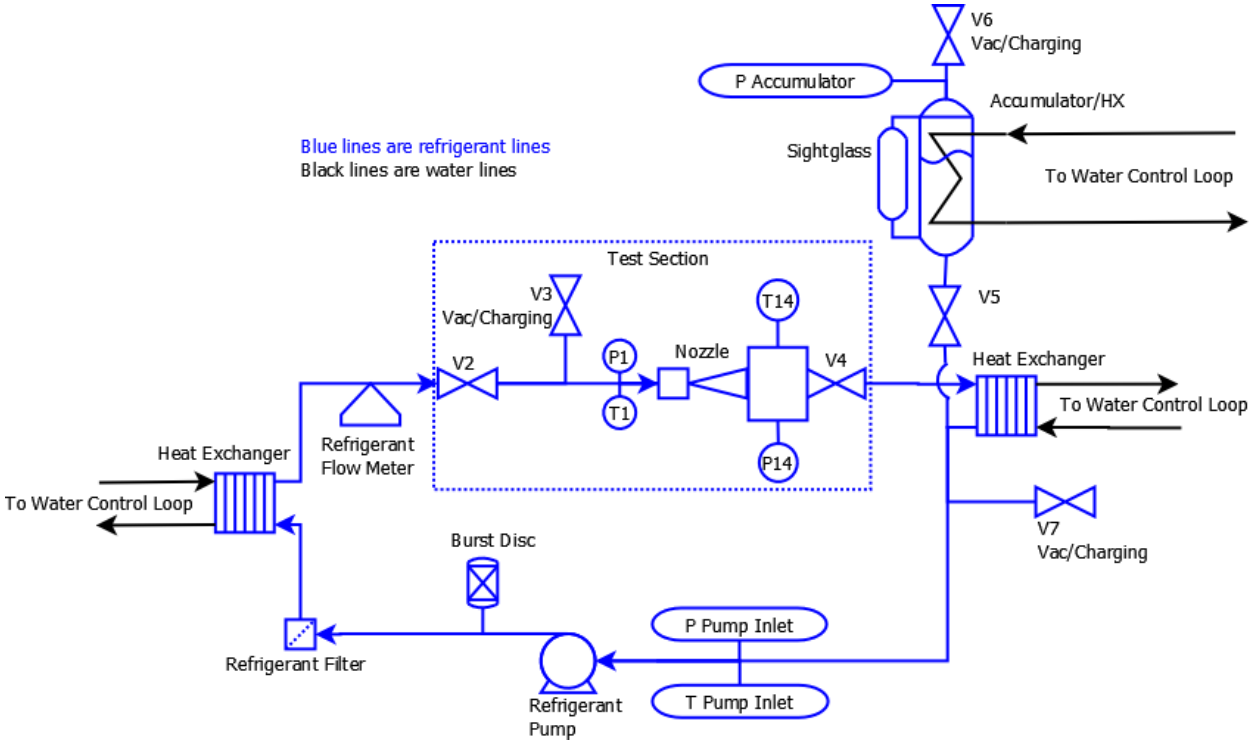

Figure 2.1: Refrigerant Loop Diagram

The inlet piping is a straight section of tubing 3/8" in diameter of at least 20 diameter's length of smooth copper pipe. The inlet pressure and temperature are measured at the beginning of the inlet piping, upstream of the throat by 20 cm. The nozzles used consist of a well-insulated aluminum converging-diverging circular nozzle of varying geometries. At the end of the nozzle, the flow enters into a rapid expansion chamber comprised of a pipe 4 inches in diameter by approximately 8 inches long. The purpose of this chamber is to provide a low velocity region after the nozzle to ensure the fluid has condensed back into a liquid before returning to the refrigerant loop pump.

All nozzles have a smooth decrease in area up to the throat followed by a conical divergent profile, with straight walls from the throat to the exit. Shown below in Figure 2.2 is a diagram defining nozzle dimensions, with definitions listed in Table 2.1.

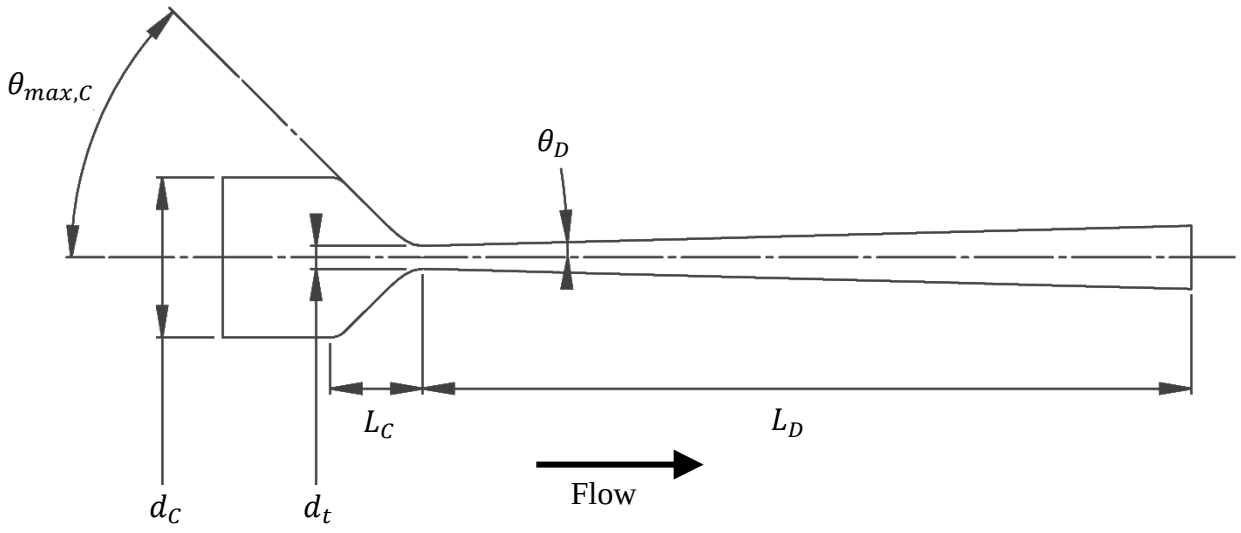

Figure 2.2: Simplified Nozzle Diagram

In addition to the above dimensions, another factor to consider in the performance of the nozzle is the addition in two test cases of an inlet flow modifier (IFM). The IFM is a device placed upstream of the throat designed to impart a rotational motion to the flow about the center

axis. The dimension noted in Table 2.1 for IFM location denotes the distance between the tip of the end of the IFM and the throat of the nozzle. A representation of the IFM is shown in Figure 2.3 with a section removed to show its internal shape.

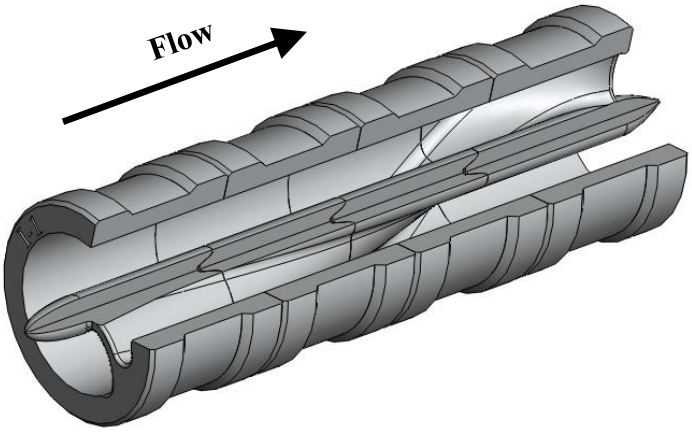

Figure 2.3: Inlet Flow Modifier

As can be seen above, the IFM is designed to induce a gradually increasing rotation in the flow for the purpose of inducing a lower pressure region within the flow near the center of the nozzle as the flow goes through the throat. The goal of this low pressure region is to further create a metastable condition within the flow, potentially extending the length of the sonic section.

Table 2.1: Nozzle Dimensions and Properties

Dimension	Description	Nozzle A	Nozzle B	Nozzle C	Nozzle D
$\theta_{max,C}$	Maximum angle of converging section (degrees)	45.0	45.0	45.0	45.0
d_C	Beginning diameter of converging section (mm)	9.52	9.52	9.52	9.52
L_C	Length of converging section (mm)	6.00	6.00	6.00	6.00
d_t	Throat diameter (mm)	1.50	1.50	1.50	1.50
θ_D	Angle of expansion, straight walls (degrees)	1.50	1.50	1.50	1.00
L_D	Length of diverging section (mm)	152	152	152	272
IFM	Inlet Flow Modifier upstream of throat?	No	Yes	Yes	No
$IFM\ Location$	Distance from end of IFM to throat (mm)	NA	17.17	9.17	NA

For this paper, four nozzles are considered. Nozzles A, B, and C have identical geometry with the exception of IFM inclusion and position. Nozzles B and C both have the IFM positioned upstream of the throat, but with Nozzle C the IFM is 8 mm closer to Nozzle B's 17.17 mm from the throat. Nozzle D has the same inlet geometry as the other nozzles, though it expands at an angle of 1° compared with the other nozzles' 1.5°. Nozzle D also has a length of 272 mm compared with the other nozzles' 152 mm. Nozzle D, like Nozzle A, does not use the IFM upstream of the throat.

According to manufacturing considerations, pressure taps were place at intermittent locations along the length of the nozzle. These taps have two forms. One form allows pressure to be measured through the gaps between sections, while the other form senses through flush holes with a diameter of 0.26 mm that pierce the nozzle walls. Both forms are represented in Figure 2.4.

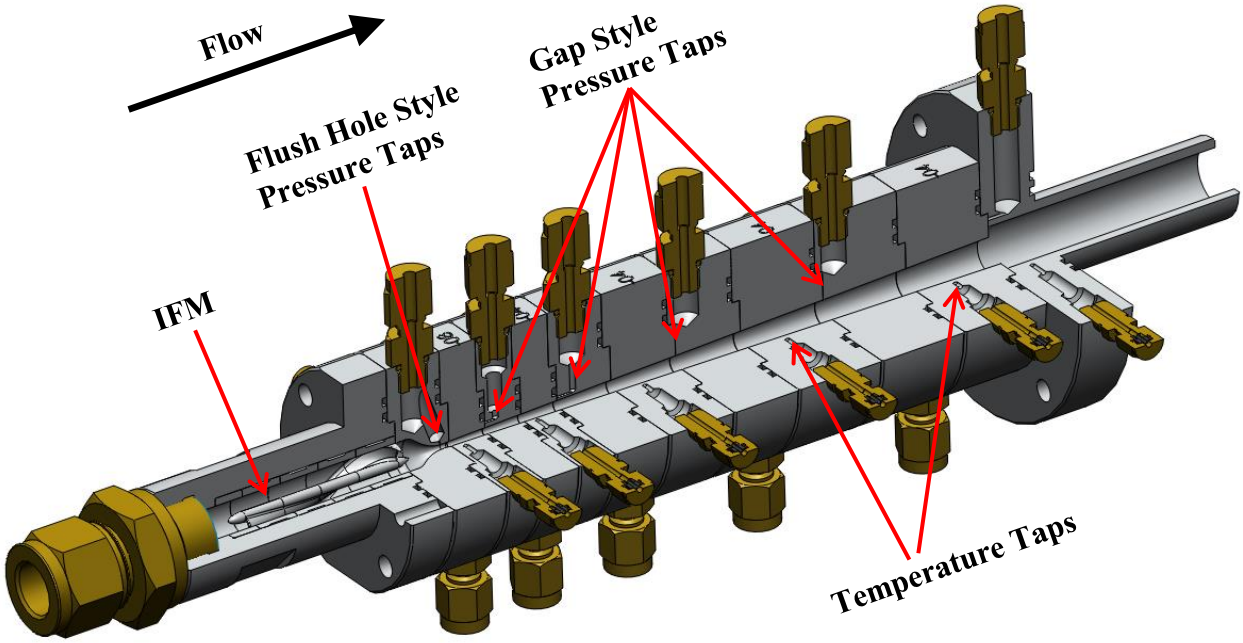

Figure 2.4: Nozzle Section Showing Pressure and Temperature Taps and IFM

Pressure is sensed by strain-gage type transducers with an uncertainty of 0.08% of full scale output. The same model of pressure transducer is also used to measure pressure in the inlet piping and in the expansion chamber, with the expansion chamber sensor being located approximately 10 inches downstream of the nozzle exit. At intermittent locations down the length of the nozzle ungrounded K-type thermocouples in temperature taps like those shown in Figure 2.4 are used to measure temperature. The thermocouples are located 0.66 mm from the flow in the nozzle wall and are contained within sheaths 1/32 inch in diameter. The same model

thermocouples were also used in the inlet piping and expansion chamber, though the diameter of the sheaths is 1/8 inch.

2.2 Refrigerant Loop

Downstream of the test section, refrigerant passes through a brazed-plate heat exchanger in order to exchange heat with the chilled water loop and condense any remaining vapor. Directly following the heat exchanger, the refrigerant piping connects with a temperature controlled, insulated accumulator. This accumulator sits above the rest of the refrigerant piping and a liquid-vapor interface is maintained within. Therefore, control of the temperature within the accumulator allows for control of the pressure of the refrigerant between the test section and the pump. Combined with the heat removal after the test section, the controlled pressure due to the accumulator serves to ensure that the refrigerant is subcooled sufficiently to maintain the required head of the main pump. In addition, this allows for back pressures at the nozzle above the required suction head of the pump. The temperature in the accumulator is controlled by an additional water loop that passes water through a coil within the accumulator.

Following the connection with the accumulator, the refrigerant reaches the main pump. The diaphragm-style positive displacement pump is powered by a three-phase motor controlled by a variable frequency drive. Control of the VFD allows for control of the mass flow and indirectly the nozzle pressure. Following the pump, the refrigerant passes through a filter on its way to another brazed-plate heat exchanger. This heat exchanger is used to raise the temperature of the refrigerant to the desired temperature necessary for test conditions before the refrigerant enters the test section. This heat exchanger connects with the hot water loop.

After the hot water heat exchanger, the refrigerant passes through a coriollis flow meter. This meter has uncertainties of ±0.05% of reading for flow rate and ±0.2 kg/m^3 for density.

Following the flow meter, the refrigerant passes into the test section. One thing to note is that the refrigerant is free of oil contamination.

2.3 Control Loops

Each of the water loops previously mentioned has the same general layout as shown in Figure 2.5.

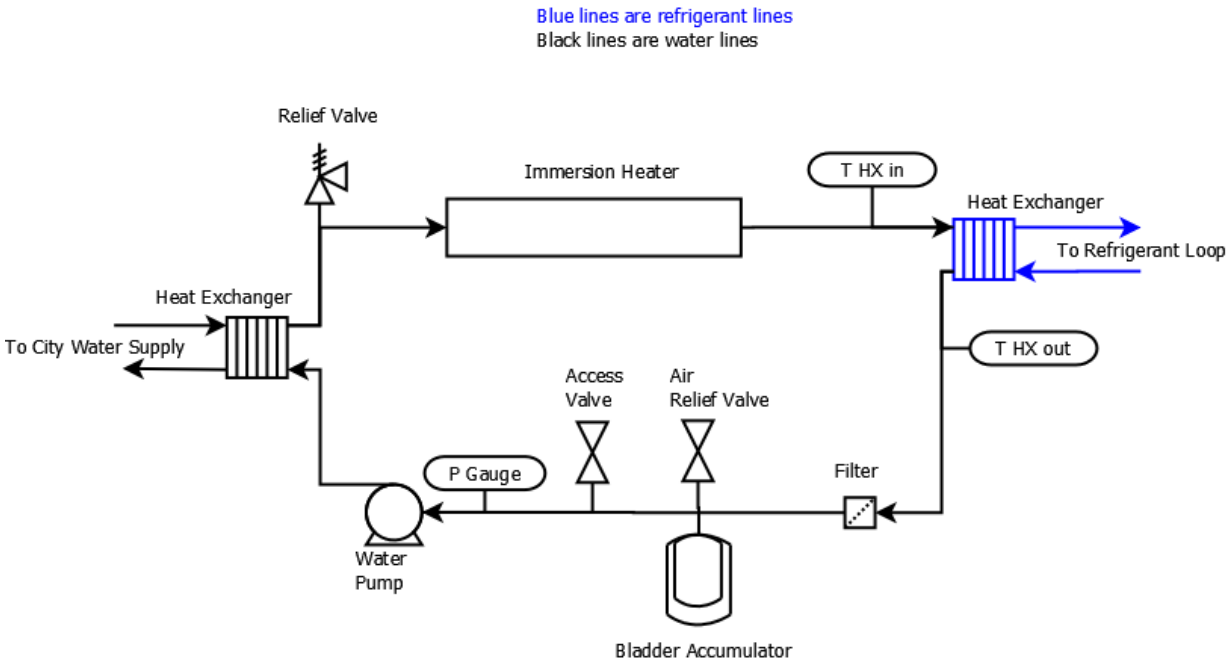

Figure 2.5: Water Loop Diagram

The only difference is each loop's purpose. Following the heat transfer with the refrigerant loop, the water in a loop flows through a filter. The water then flows back to a fixed speed centrifugal pump that moves the water to a brazed-plate heat exchanger where the water is cooled by city supplied water at approximately 15 °C. Following this heat exchanger, the water flows through a three-phase immersion heater. This heater is powered through a solid-state relay controlled by a PID temperature controller that controls based on the temperature reading from a thermocouple located downstream of the heater. The temperature controller cycles the relay on and off to

maintain the set temperature. The temperature set at the controller is adjusted to achieve the desired refrigerant temperature after each heat exchanger in the refrigerant loop. Following the heater, the water flows to the refrigerant loop heat exchanger. Air is kept out of the system by use of a pressurized bladder tank and an air relief valve. Each water loop also contains a pressure relief valve to prevent damage in case of a pump failure and subsequent local boiling in the heater. The value in these water loops is that very stable temperatures are achieved in the refrigerant loop.

2.4 Operation and Data Acquisition

The system is operated by control of the main pump's speed through the VFD and by setting the temperature controllers to achieve the desired conditions. Systems conditions are monitored through use of a LabView virtual instrument and adjusted through manually setting the controls listed above. The system is brought to steady-state conditions and then data is taken at 5 second intervals for 10 points. The VI takes the raw measurements from a data acquisition unit and scales and adjusts the signals according to calibration. The corrected data is then recorded to a text file for later processing in a spreadsheet.

2.5 Calibration

For this system, pressure transducers were calibrated in two ways. Before installation in the system, all transducers were calibrated with a pneumatic deadweight tester referenced to a NIST traceable digital barometer, with the transducer voltage readings fitted to pressure values using a second order polynomial. After installation, the pressure transducers in the test section were intermittently checked and calibration was adjusted at room pressure with an offset using the same digital barometer.

The thermocouples were calibrated before installation using a constant temperature bath calibrated to a NIST traceable mercury thermometer, using an offset. After installation the thermocouples were intermittently removed and checked using the constant temperature bath. For the coriolis flow meter, the factory calibration was used, though verified using a stopwatch and bucket.

Chapter 3 - Theoretical Analysis

In order to model and analyze two-phase flow with friction, it was decided to employ equations of conservation of mass, momentum, and energy. As stated in Chapter 1, a majority of models involving two-phase flow have been developed with any conservation equations in differential form. In order to analyze the data acquired during the current experiments, it is more useful to apply the integral forms of these equations. Also, as most models are developed for constant area ducts, in developing the equations from their basic forms, we are able to include terms in our equations that resolve the variable area of converging-diverging nozzles that are lacking in current models.

3.1 Basic Conservation Equations

Before we can begin to develop the HEM and separated flow model, it is necessary to first derive the basic conservation equations that are common between them. For this, we consider a control volume consisting of a circular duct of variable cross-sectional area as shown in Figure 3.1. Fluid flows from the left side of the duct to the right, along the positive z-axis. The control volume is assumed to be stationary, well-insulated, horizontal, and flow is further assume to be steady-state. We also assume average fluid properties and values across the duct. In other words, the properties such as density, pressure, and velocity are constant at a given location z even with varying radius r. As such, we are essentially assuming one-dimensional flow. The duct's axis is set to be in the z-direction with unit vector $\vec{k}$.

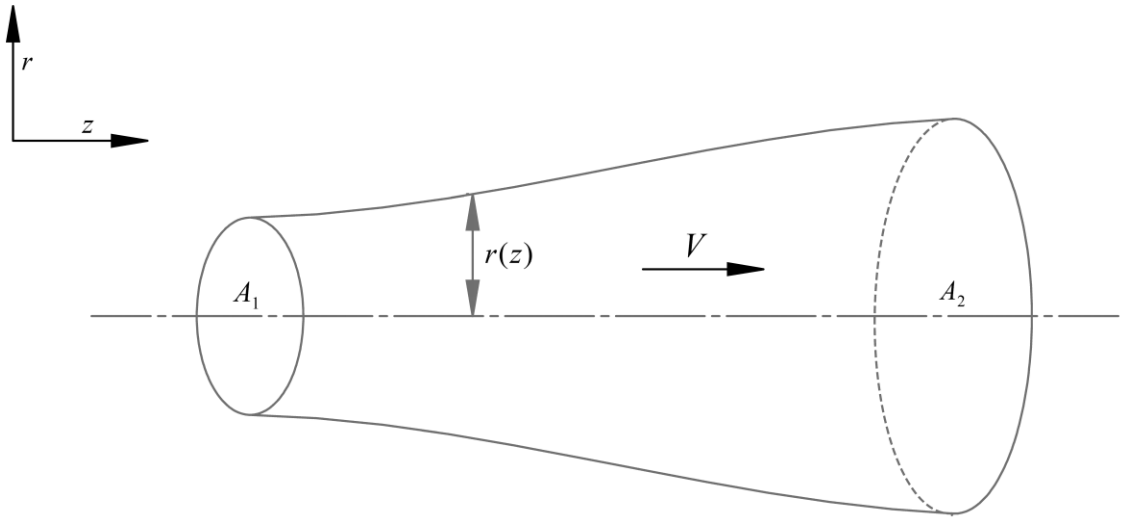

Figure 3.1: Horizontal Circular Duct of Variable Area

Conservation of Mass

We begin from the basic equation of conservation of mass

$$\frac{dMa}{dt}\Big)_{system} = 0 \qquad [3.1]$$

where Ma is the total mass of the system (Fox, McDonald et al. 2006). Obtaining the first part of [3.1] for the the control volume of Figure 3.1 results in

$$\frac{dMa}{dt}\Big)_{system} = \frac{\partial}{\partial t}\int_{CV} \rho \, d\forall + \int_{CS} \rho \, \vec{V} \cdot d\vec{A} \qquad [3.2]$$

where ρ is density and $\forall$ is volume. Combining [3.1] and [3.2] and applying the assumption of steady-state conditions (no change of mass in the control volume), results in

$$\int_{CS} \rho \, \vec{V} \cdot d\vec{A} = 0 \qquad [3.3]$$

in which we have dropped the term concerning the rate of change with time. As we are assuming a one-dimensional form and neglecting any flow not perpendicular to the inlet and exit areas, this simplifies further to

$$\rho_2 V_2 A_2 - \rho_1 V_1 A_1 = \dot{m}_2 - \dot{m}_1 = 0 \quad [3.4]$$

in which we essentially state that the mass flow through the inlet is the same as the mass flow through the outlet. As such, the equation simplifies finally to

$$\dot{m}_1 = \dot{m}_2 = \dot{m} = constant. \quad [3.5]$$

Conservation of Momentum

To develop the equations of conservation of momentum, it is useful to begin from Newton's second law with the form

$$\vec{F} = \frac{d\vec{P}}{dt}\Big)_{system} \quad [3.6]$$

in which the resultant force on the system is equal to the change in linear momentum (Fox, McDonald et al. 2006). The forces acting on the control volume are represented as

$$\vec{F} = \vec{F}_{body} + \vec{F}_{surface} \quad [3.7]$$

with the change in momentum given by

$$\frac{d\vec{P}}{dt}\Big)_{system} = \frac{\partial}{\partial t}\int_{CV} \vec{V}\,\rho\, d\forall + \int_{CS} \vec{V}\,\rho\,\vec{V}\cdot d\vec{A}. \quad [3.8]$$

Substituting [3.7] and [3.8] into [3.6] yields

$$\vec{F}_{body} + \vec{F}_{surface} = \frac{\partial}{\partial t}\int_{CV} \vec{V}\,\rho\, d\forall + \int_{CS} \vec{V}\,\rho\,\vec{V}\cdot d\vec{A}. \quad [3.9]$$

It is useful at this point to look at each term of [3.9] individually and irrespective of the coordinate system and then develop the necessary equations for the horizontal orientation. As our control volume is at rest, the only body force acting upon it is gravity

$$\vec{F}_{body} = \int_{CV} \rho \, \vec{g} \, d\forall \qquad [3.10]$$

and can thus be dropped completely as we are considering only the forces along the horizontal axis.

The surface forces are the result of pressure and shear stress on the walls of the control volume, given by

$$\vec{F}_{surface} = -\int_{CS} p \, d\vec{A} - \int_{CS} \vec{\tau} \, dA \qquad [3.11]$$

with the positive direction of $d\vec{A}$ being from the inside of the control volume outwards, p denoting pressure, and τ denoting the shear stress. As we are assuming the one-dimensional flow, the pressure is uniform across the circular cross section at each location z along the nozzle's axis, including the inflow and outflow surfaces. As such, we can split the second term up as follows

$$\vec{F}_{surface} = -(p_2 A_2 - p_1 A_1)\vec{k} - \int_{sides} p \, d\vec{A} - \int_{sides} \vec{\tau} \, dA. \qquad [3.12]$$

Now let us consider only the forces in the z-direction. This leaves us with

$$F_{surface,z} = -(p_2 A_2 - p_1 A_1) + 2\pi \int_1^2 p(z) r(z) \frac{dr}{dz} dz - 2\pi \int_1^2 \tau_z(z) \, r(z) dz \qquad [3.13]$$

which for a predictive application of our model requires us to know both the pressure distribution and shear distribution as a function of position z.

For the third term of [3.9], as we assume steady state, the momentum of the control volume is constant and the partial derivative with time goes to zero. As such, this term drops out.

For the final term of [3.9], we can recognize that at each location z we consider density and velocity uniform across the corresponding cross section A. As such, the final term can be simplified to

$$\int_{CS} \vec{V}\, \rho\, \vec{V} \cdot d\vec{A} = \vec{V}_2 \rho_2 V_2 A_2 - \vec{V}_1 \rho_1 V_1 A_1. \quad [3.14]$$

Taking only the components in the z-direction and applying our equation for conservation of mass, we simplify further and get

$$\int_{CS,z} V\, \rho\, V\, dA = \dot{m}(V_2 - V_1). \quad [3.15]$$

Finally, we can combine [3.13] and [3.15] into [3.9] for the components in the z-direction, yielding

$$-(p_2 A_2 - p_1 A_1) + 2\pi \int_1^2 p(z) r(z) \frac{dr}{dz} dz - 2\pi \int_1^2 \tau(z)\, r(z) dz = \dot{m}(V_2 - V_1). \quad [3.16]$$

[3.16] forms the basic integral conservation of momentum equation the control volume.

Conservation of Energy

Considering the control volume shown in Figure 3.1, we construct an energy balance based off of the first law of thermodynamics (Fox, McDonald et al. 2006) as

$$\dot{Q} - \dot{W} = \frac{\partial}{\partial t} \int_{CV} \left(h + \frac{V^2}{2} + gr \right) \rho d\forall + \int_{CS} \left(h + \frac{V^2}{2} + gr \right) \rho \vec{V} \cdot d\vec{A}. \quad [3.17]$$

Looking at each term, this equation simplifies much further. The heat transfer term $\dot{Q}$ drops out as we are assuming adiabatic walls. The work term $\dot{W}$ is eliminated as no work occurs on or by

the control volume of constant volume and location. The third term involving the rate of change over time drops out as we are assuming steady state. As our flow is horizontal, there is no potential energy due to gravity between the two states and we can drop the term involving gravity. As such, we are left simply with

$$\int_{CS} \left(h + \frac{V^2}{2}\right) \rho \vec{V} \cdot d\vec{A} = 0. \quad [3.18]$$

[3.18] is expanded to

$$\int_{CS} \left(h + \frac{V^2}{2}\right) \rho \vec{V} \cdot d\vec{A} = \rho_2 V_2 A_2 \left(h_2 + \frac{V_2^2}{2}\right) - \rho_1 V_1 A_1 \left(h_1 + \frac{V_1^2}{2}\right) \quad [3.19]$$

in which our assumption of one-dimensional flow across the outlets of the control volume means that enthalpy, velocity, and density are constant across the inlet and outlet respectively. We then apply [3.4] and [3.5] to finally yield

$$\rho_2 V_2 A_2 \left(h_2 + \frac{V_2^2}{2}\right) - \rho_1 V_1 A_1 \left(h_1 + \frac{V_1^2}{2}\right) = \dot{m} \left(h_2 - h_1 + \frac{1}{2}(V_2^2 - V_1^2)\right) = 0. \quad [3.20]$$

At this point it is possible to apply our basic equations to the models of interest as described in Section 1.4.

3.2 Homogeneous Equilibrium Model Conservation Equations

With the equations of Section 3.1, we can now modify the equations of conservation of mass, energy, and momentum to more specifically apply to the homogeneous equilibrium model. Before that, though, the assumptions of the HEM should be restated:

- Flow is in thermal equilibrium
- Flow is in mechanical equilibrium

Thermal equilibrium denotes that both liquid and vapor phases have the same pressure and temperature at any given location and mechanical equilibrium denotes that both phases move with the same velocity.

In applying the conservation equations to the HEM, we denote x as the quality of the fluid and α as the void fraction, with each being defined by

$$x = \frac{\dot{m}_v}{\dot{m}} = 1 - \frac{\dot{m}_l}{\dot{m}} \quad [3.21]$$

and

$$\alpha = \frac{A_v}{A} = 1 - \frac{A_l}{A} \quad [3.22]$$

where the subscripts v and l denote vapor and liquid, respectively (Levy 1999). It is also necessary to note that the liquid and vapor densities can be related to the bulk density by the relation

$$\frac{1}{\rho} = \frac{1-x}{\rho_l} + \frac{x}{\rho_v} \ . \quad [3.23]$$

With the quality and void fraction defined, we can modify [3.4] to get

$$\dot{m}_{1,l} + \dot{m}_{1,v} = \dot{m}_{2,l} + \dot{m}_{2,v} \quad [3.24]$$

whose components are

$$\rho_{1,l}V_{1,l}A_{1,l} + \rho_{1,v}V_{1,v}A_{1,v} = \rho_{2,l}V_{2,l}A_{2,l} + \rho_{2,v}V_{2,v}A_{2,v}. \quad [3.25]$$

As the flow is in mechanical equilibrium, $V_l = V_v$ and [3.25] becomes

$$V_1(\rho_{1,l}A_{1,l} + \rho_{1,v}A_{1,v}) = V_2(\rho_{2,l}A_{2,l} + \rho_{2,v}A_{2,v}). \quad [3.26]$$

Applying [3.22] to [3.26] allows us to reduce this further to

$$V_1(\rho_{1,l}(1-\alpha_1) + \rho_{1,v}\alpha_1) = V_2(\rho_{2,l}(1-\alpha_2) + \rho_{2,v}\alpha_2). \quad [3.27]$$

For the momentum equation, we simply use the given form of [3.16] to get

$$-(p_2A_2 - p_1A_1) + 2\pi \int_1^2 p(z)r(z)\frac{dr}{dz}dz - 2\pi \int_1^2 \tau(z)\, r(z)dz = \dot{m}(V_2 - V_1) \quad [3.28]$$

as all terms as shown are irrespective of void fraction or quality.

For the energy equation, we apply [3.21] to [3.20] to yield

$$\dot{m}\left(x_2h_{2,v} - x_1h_{1,v} + (1-x_2)h_{2,l} - (1-x_1)h_{1,l} + \frac{1}{2}(V_2^2 - V_1^2)\right) = 0. \quad [3.29]$$

3.3 Separated Flow Model Conservation Equations

The separated flow model allows for a potentially more accurate model of sonic, two-phase flow than the HEM. With the equations of Sections 3.1 and 3.2 we can now modify the equations of conservation of mass, momentum, and energy to more specifically apply to the homogeneous equilibrium model. Again, as with the HEM, it is useful to restate the necessary assumptions for separated flow:

- Flow is in thermal equilibrium
- The flow has a variable S, defined as the ratio of the vapor velocity to liquid velocity

As with the HEM, thermal equilibrium denotes that both liquid and vapor phases have the same pressure and temperature at any given location. However, the second assumption allows for the vapor velocity to reach velocities much faster than the liquid velocity at a given location, dependent on quality and void fraction.

In developing the conservation equations for the separated flow model, it is useful to initially treat the control volume in Figure 3.1 as two adjacent, yet separate control volumes: one containing only the liquid portion of the flow and the other containing only the vapor. This allows us to take into account the interfacial forces and mass transfer occurring between the two

phases. Mass is allowed to pass between the phases as is force, treating the wall between the two control volumes as flexible and porous.

We develop the conservation equations by recognizing the definition of the slip ratio S as stated by [1.4] to denote the ratio between the liquid and vapor phases and is given by

$$S = \frac{V_v}{V_l} = \left(\frac{\rho_l}{\rho_v}\right)^n. \quad [3.30]$$

and further defined by the ratio of the liquid to vapor densities raised to a power n. Note again that for $S = 1$, we again see $V_v = V_l = V$, meaning that the separated flow model becomes equivalent to the HEM. This occurs for $n = 0$. Note also that [3.21] and [3.22] of Section 3.2 also apply to the separated flow model.

For the conservation of mass, treating the liquid and vapor as adjacent, yet separate control volumes, we get the following equations:

$$\dot{m}_{1,l} + \dot{m}_{v\to l} = \dot{m}_{2,l} \quad [3.31]$$

$$\dot{m}_{1,v} + \dot{m}_{l\to v} = \dot{m}_{2,v} \quad [3.32]$$

and recognize that the relationship of mass transfer between control volumes is given by

$$\dot{m}_{l\to v} = -\dot{m}_{v\to l}. \quad [3.33]$$

Applying [3.33] and adding together the control volumes, [3.31] and [3.32] combine to form

$$\dot{m}_{1,l} + \dot{m}_{v\to l} + \dot{m}_{1,v} + \dot{m}_{l\to v} = \dot{m}_{2,l} + \dot{m}_{2,v} \quad [3.34]$$

Expanding [3.34] and applying [3.4] and [3.33] gives us

$$\rho_{1,l}V_{1,l}A_{1,l} + \rho_{1,v}V_{1,v}A_{1,v} = \rho_{2,l}V_{2,l}A_{2,l} + \rho_{2,v}V_{2,v}A_{2,v}. \quad [3.35]$$

We then apply both [3.30] and [3.22] to [3.35] and shift all variables to one side of the equation, which finally gives us

$$A_2V_{2,l}\left((1-\alpha_2)\rho_{2,l} + \alpha_2\rho_{2,v}S_2\right) - A_1V_{1,l}\left((1-\alpha_1)\rho_{1,l} + \alpha_1\rho_{1,v}S_1\right) = 0. \quad [3.36]$$

For the conservation of momentum, it is useful to begin from a modified form of [3.9] instead of the simplified [3.16]:

$$\vec{F}_{surface,l} = \int_{CS,l} \vec{V}\,\rho\,\vec{V}\cdot d\vec{A} \qquad [3.37]$$

$$\vec{F}_{surface,v} = \int_{CS,v} \vec{V}\,\rho\,\vec{V}\cdot d\vec{A} \qquad [3.38]$$

making the same simplifications with regards to body forces and steady state flow. Expanding [3.37] and [3.38] as was done in Section 3.1 yields

$$-\int_{CS,l\to v} p\,d\vec{A} - \int_{CS,l\to v} \vec{\tau}\,dA - \int_{CS,l\to wall} p\,d\vec{A} - \int_{CS,l\to wall} \vec{\tau}\,dA = \int_{CS,l\to outlets} \vec{V}_l\,\rho_l\,\vec{V}_l\cdot d\vec{A} + \vec{V}_{l\to v}\dot{m}_{l\to v} \qquad [3.39]$$

and

$$-\int_{CS,v\to l} p\,d\vec{A} - \int_{CS,v\to l} \vec{\tau}\,dA - \int_{CS,v\to wall} p\,d\vec{A} - \int_{CS,v\to wall} \vec{\tau}\,dA = \int_{CS,v\to outlets} \vec{V}_v\,\rho_v\,\vec{V}_v\cdot d\vec{A} + \vec{V}_{v\to l}\dot{m}_{v\to l} \qquad [3.40]$$

where we have separated the pressure and shear terms to involve the interfacial portion between the control volumes and also the portion that acts upon the walls and outlets. The momentum side of the equations has also been separated into the flow across the interface and the flows across the inlet and outlet. As per Collier and Thome (1994), conservation of momentum across the interface requires that

$$\int_{CS,l\to v} p\,d\vec{A} + \int_{CS,l\to v} \vec{\tau}\,dA + \vec{V}_{l\to v}\dot{m}_{l\to v} \qquad [3.41]$$

$$= \int_{CS,v\to l} p\, d\vec{A} + \int_{CS,v\to l} \vec{\tau}\, dA + \vec{V}_{v\to l}\dot{m}_{v\to l}.$$

Further realizing that with our assumption of thermal equilibrium, pressure is equal on either side of the interface

$$\int_{CS,l\to v} p\, d\vec{A} = \int_{CS,v\to l} p\, d\vec{A} \qquad [3.42]$$

and we are left with

$$\int_{CS,l\to v} \vec{\tau}\, dA + \vec{V}_{l\to v}\dot{m}_{l\to v} = \int_{CS,v\to l} \vec{\tau}\, dA + \vec{V}_{v\to l}\dot{m}_{v\to l}. \qquad [3.43]$$

As such, when we combine [3.39] and [3.40], the interfacial shear and momentum exchange terms drop out

$$-\int_{CS,l\to wall} p\, d\vec{A} - \int_{CS,v\to wall} p\, d\vec{A} - \int_{CS,l\to wall} \vec{\tau}\, dA - \int_{CS,v\to wall} \vec{\tau}\, dA = \int_{CS,l} \vec{V}_l\, \rho_l\, \vec{V}_l \cdot d\vec{A} + \int_{CS,v} \vec{V}_v\, \rho_v\, \vec{V}_v \cdot d\vec{A}. \qquad [3.44]$$

Since the pressure is uniform at any given location z, we can combine the liquid and vapor pressure terms and take the pressure over the entirety of the control volume's walls, giving us the same pressure terms as [3.16]. For convenience, we do the same for the shear terms, even though the two phases will have different values of shear due to differing viscosities, velocities, and effective area at the walls. This action gives us a combined liquid and vapor shear term. Applying these simplifications, taking only the components along the z-direction, and evaluating the integrals on the right side of [3.44] yields

$$-(p_2A_2 - p_1A_1) + 2\pi\int_1^2 p(z)r(z)\frac{dr}{dz}dz - 2\pi\int_1^2 \tau(z)\, r(z)dz$$
$$= V_{2,l}\rho_{2,l}V_{2,l}A_{2,l} + V_{2,v}\rho_{2,v}V_{2,v}A_{2,v} - V_{1,l}\rho_{1,l}V_{1,l}A_{1,l} - V_{1,v}\rho_{1,v}V_{1,v}A_{1,v}. \quad [3.45]$$

Applying [3.4] and [3.30] and shifting all variables to one side of the equation, this equation becomes

$$p_2A_2 - p_1A_1 - 2\pi\int_1^2 p(z)r(z)\frac{dr}{dz}dz + 2\pi\int_1^2 \tau(z)\, r(z)dz$$
$$+ \dot{m}\left[V_{2,l}\left((1-x_2) + S_2x_2\right) - V_{1,l}\left((1-x_1) + S_1x_1\right)\right] = 0 \quad [3.46]$$

giving us our conservation of momentum equation for the separated flow model.

As with the conservation of momentum, for the conservation of energy it is useful to start from a more general case than [3.20]. We begin by applying [3.18] to both the liquid and vapor control volumes, but including a term in each to account for energy transfer due to mass transfer across the interface. This gives us

$$\int_{CS,l}\left(h_l + \frac{{V_l}^2}{2}\right)\rho_l\overrightarrow{V_l}\cdot d\vec{A} + \dot{m}_{l\to v}h_{lv} = 0 \quad [3.47]$$

and

$$\int_{CS,v}\left(h_v + \frac{{V_v}^2}{2}\right)\rho_v\overrightarrow{V_v}\cdot d\vec{A} + \dot{m}_{v\to l}h_{lv} = 0 \quad [3.48]$$

Note that these equations ignore the kinetic energy portion of mass transfer, as our one dimensional model ignores the velocity across the interface. Applying [3.33] to eliminate the energy transfer due to mass transfer and combining [3.47] and [3.48] by combining the control volumes yields

$$\int_{CS,l}\left(h_l + \frac{{V_l}^2}{2}\right)\rho_l\vec{V}_l\cdot d\vec{A} + \int_{CS,v}\left(h_v + \frac{{V_v}^2}{2}\right)\rho_v\vec{V}_v\cdot d\vec{A} = 0. \quad [3.49]$$

Evaluating the integrals gives us

$$\left(h_{2,l}+\frac{1}{2}V_{2,l}^2\right)\rho_{2,l}V_{2,l}A_{2,l}-\left(h_{1,l}+\frac{1}{2}V_{1,l}^2\right)\rho_{1,l}V_{1,l}A_{1,l}$$
$$+\left(h_{2,v}+\frac{1}{2}V_{2,v}^2\right)\rho_{2,v}V_{2,v}A_{2,v}-\left(h_{1,v}+\frac{1}{2}V_{1,v}^2\right)\rho_{1,v}V_{1,v}A_{1,v}=0 \quad [3.50]$$

and we then apply [3.4], [3.21], and [3.30] to get

$$\dot{m}\left[(1-x_2)\left(h_{2,l}+\frac{V_{2,l}^2}{2}\right)+x_2\left(h_{2,v}+\frac{\left(S_2V_{2,l}\right)^2}{2}\right)-(1-x_1)\left(h_{1,l}+\frac{V_{1,l}^2}{2}\right)\right.$$
$$\left.-x_1\left(h_{1,v}+\frac{\left(S_1V_{1,l}\right)^2}{2}\right)\right]=0. \quad [3.51]$$

When solved in conjunction with [3.36] and [3.46], [3.51] allows for application of the separated flow model.

3.4 Summary

With the experimental mass, pressure, and temperature data described in the next chapter and the initial conditions and data conditioning of Chapter 5, simultaneously solving the above equations will allow us to find several key variables of our flow. Among the variables to be found are velocities, qualities, void fractions, Mach numbers, and values of wall shear. These will be the variables that define sonic, two-phase flow in our nozzles in Chapter 6.

Chapter 4 - Experimental Data

In this chapter, pressure, temperature, and mass flow data from our experiments are examined without applying the models developed in Chapter 3. Due to the nature of sonic, two-phase flow, several interesting phenomena are evident even without the benefit of applying our analysis to the data.

4.1 Experiment Conditions

Data for each nozzle was taken at one inlet temperature for seven different calculated liquid throat velocities as given by $V = \dot{m}/\rho A$, where $\dot{m}$ and ρ are measured by the coriolis flow meter and A is the throat cross-sectional area calculated from the measured throat diameter. For each nozzle, a given throat velocity roughly corresponded to the same inlet pressure for all seven velocities. All experimental measurements are presented in Appendix A - , but Table 4.1 summarizes the relevant inlet temperatures, mass flow rates, and pressure test conditions for all runs.

Table 4.1: Nozzle Test Conditions

Throat Velocity	Inlet Temperature (°C)				Mass Flow Rate (kg/s)			
(m/s)	A	B	C	D	A	B	C	D
20	25.2	25.1	24.9	25.1	0.043	0.043	0.042	0.042
25	25.1	25.1	24.9	24.9	0.054	0.053	0.053	0.053
30	24.7	24.9	24.9	24.9	0.064	0.065	0.064	0.064
35	25.0	24.9	24.9	24.8	0.075	0.075	0.075	0.075
40	25.1	24.9	25.0	24.8	0.085	0.086	0.086	0.086
45	25.0	24.9	25.0	24.9	0.097	0.097	0.098	0.098
50	24.8	24.8	24.9	24.9	0.108	0.108	0.108	0.108
Throat Velocity	Inlet Pressure (kPa)				Exit Pressure (kPa)			
(m/s)	A	B	C	D	A	B	C	D
20	789	781	783	790	667	657	663	663
25	914	901	913	916	665	657	657	657
30	1080	1091	1092	1091	662	653	655	655
35	1301	1304	1305	1288	664	655	655	655
40	1540	1553	1568	1560	661	653	657	657
45	1833	1849	1867	1846	663	654	656	656
50	2152	2179	2162	2171	660	656	656	656

The similarity in inlet pressures for a given velocity is to be expected, as all nozzles tested had the exact same geometry up to the throat. The pressure drop across each nozzle follows a trend as shown in Figure 4.1

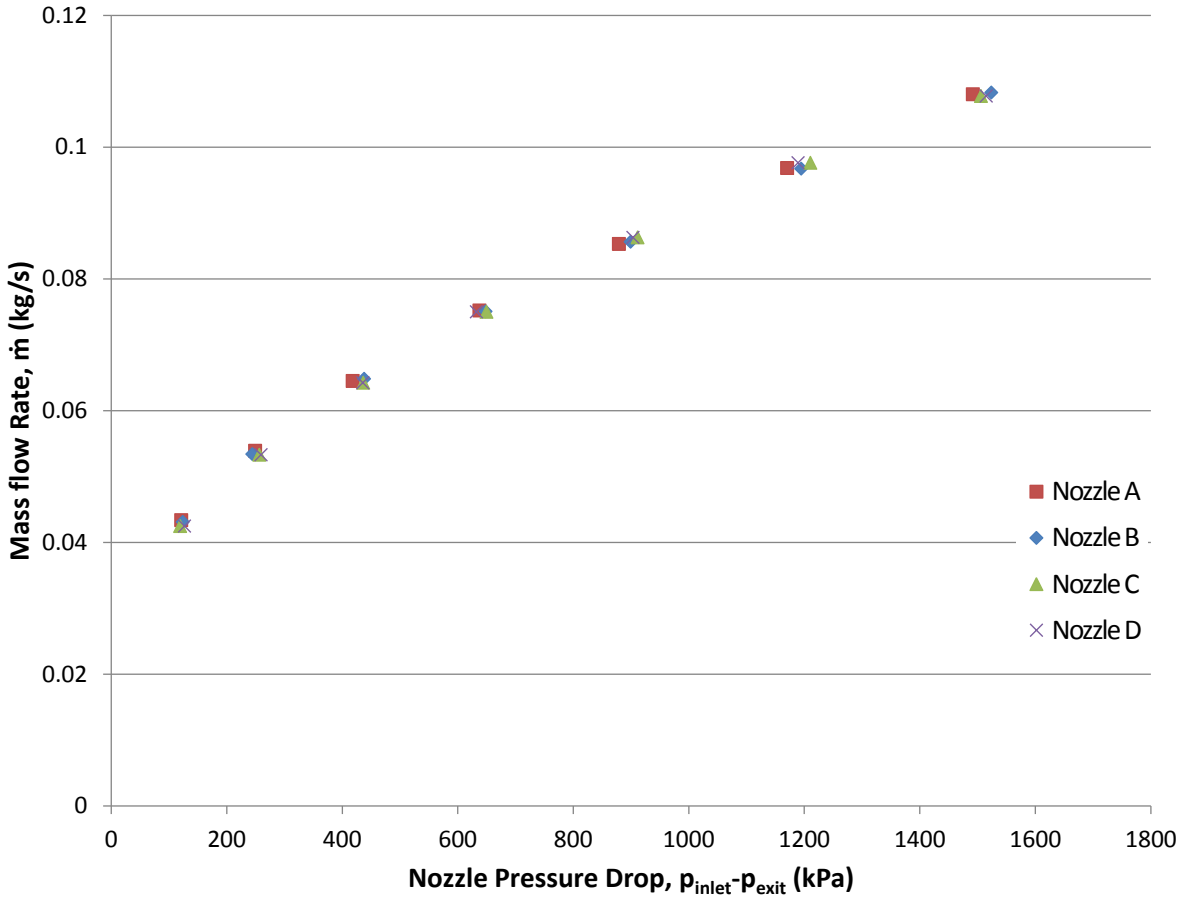

Figure 4.1: Mass Flow Rate vs Pressure Drop per Nozzle

in which $\dot{V}^2 \propto p_{inlet} - p_{exit}$, illustrating the relationship between kinetic and potential energy we would anticipate from Bernoulli's. This is to be expected, as all nozzles possess identical geometry up to the throat.

4.2 Pressure Profile

Depending on the nozzle and test conditions, several phenomena can be observed. For Nozzle A, the lowest pressure always occurs at the first pressure tap, located at 2 mm after the throat for all nozzles, with the rest of the pressures trending upward until they eventually reach the outlet pressure as shown in Figure 4.2.

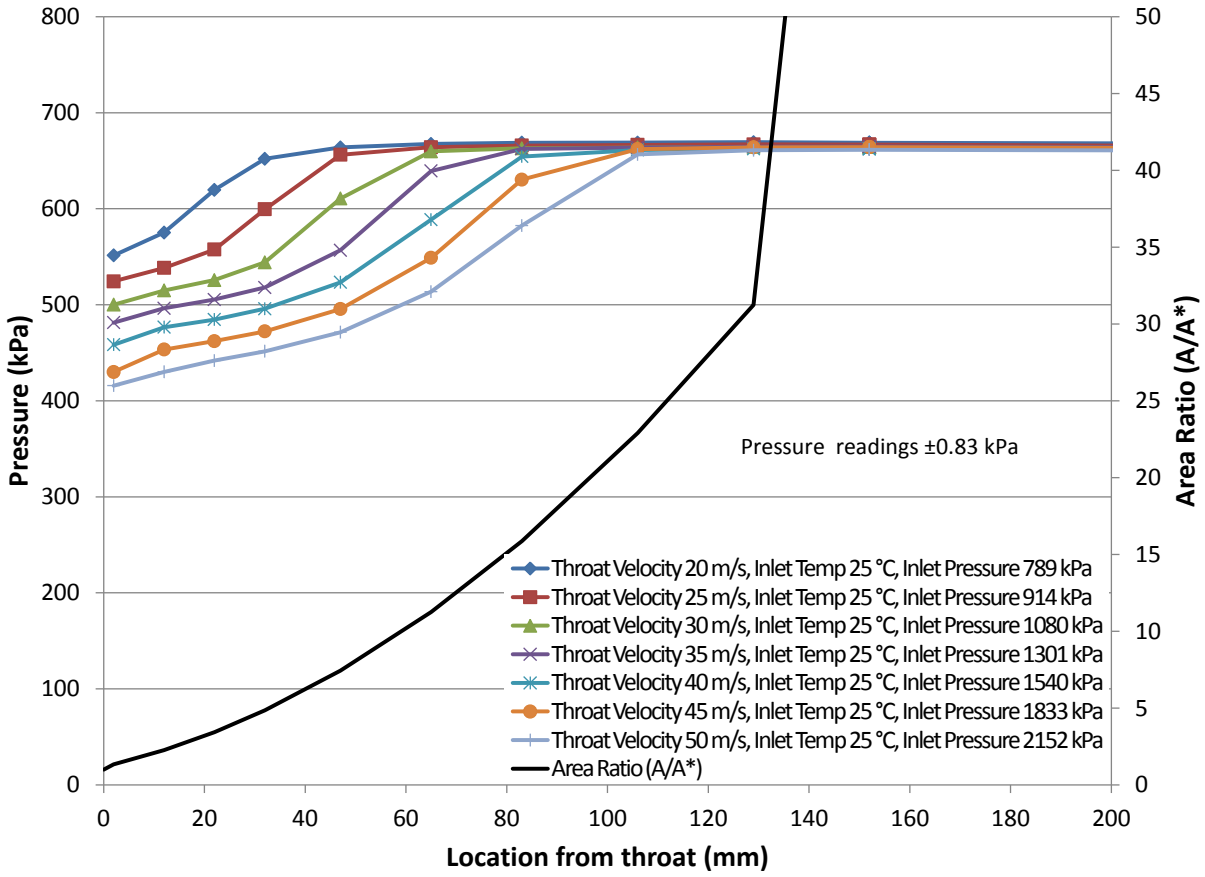

Figure 4.2: Nozzle A, Pressure vs Location

Note that the outlet pressure is slightly above the saturation pressure of the inlet temperature of 25°C. A higher throat velocity (and thus inlet pressure) results in overall lower pressures within the nozzle.

However, when we look at the pressure profile for Nozzle B in Figure 4.3, whose geometry includes an IFM, we can see a different behavior.

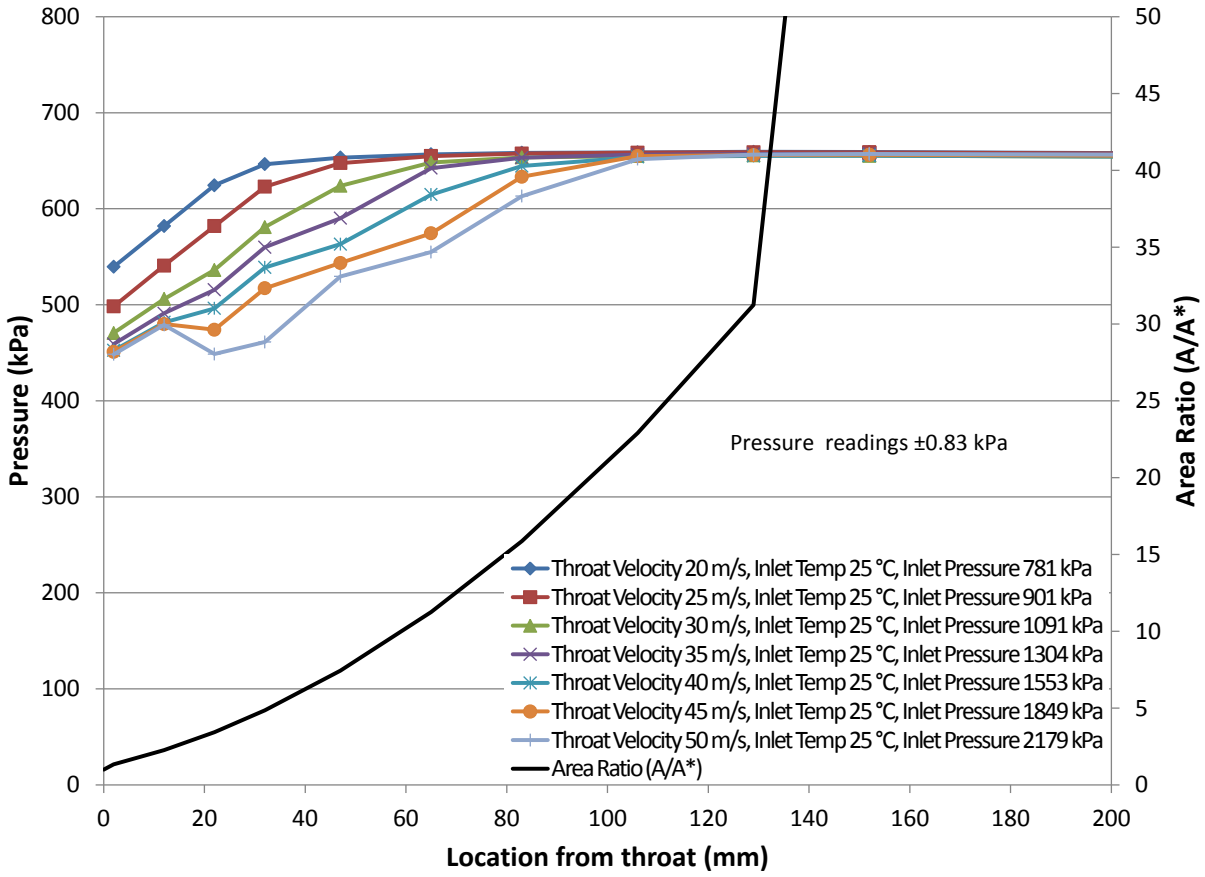

Figure 4.3: Nozzle B, Pressure vs Location

As with Nozzle A, an increase in throat velocity corresponds to lower pressures in the nozzle. However, for Nozzle B for velocities of 45 m/s and 50 m/s, we also see a drop in pressure as our area increases. This is shown by the drop in pressure at approximately 20 mm. The pressures for those velocities then return to the saturation pressure further down the nozzle, but for a section, $dp/dz < 0$ for a duct of increasing area. This negative pressure gradient in expanding flow is not possible unless the flow is two-phase and sonic. Examining the pressure profile of Nozzle C in Figure 4.4, we see the same behavior, though the decreasing pressure region extends deeper and further than with Nozzle B. The lowest measured pressure in Nozzle C occurs not near the throat at the first tap, but rather at the fourth tap, 32 mm from the throat. Nozzles B and

C possess the same geometry with the exception of the IFM placement, which for Nozzle C is 8 mm closer to the throat.

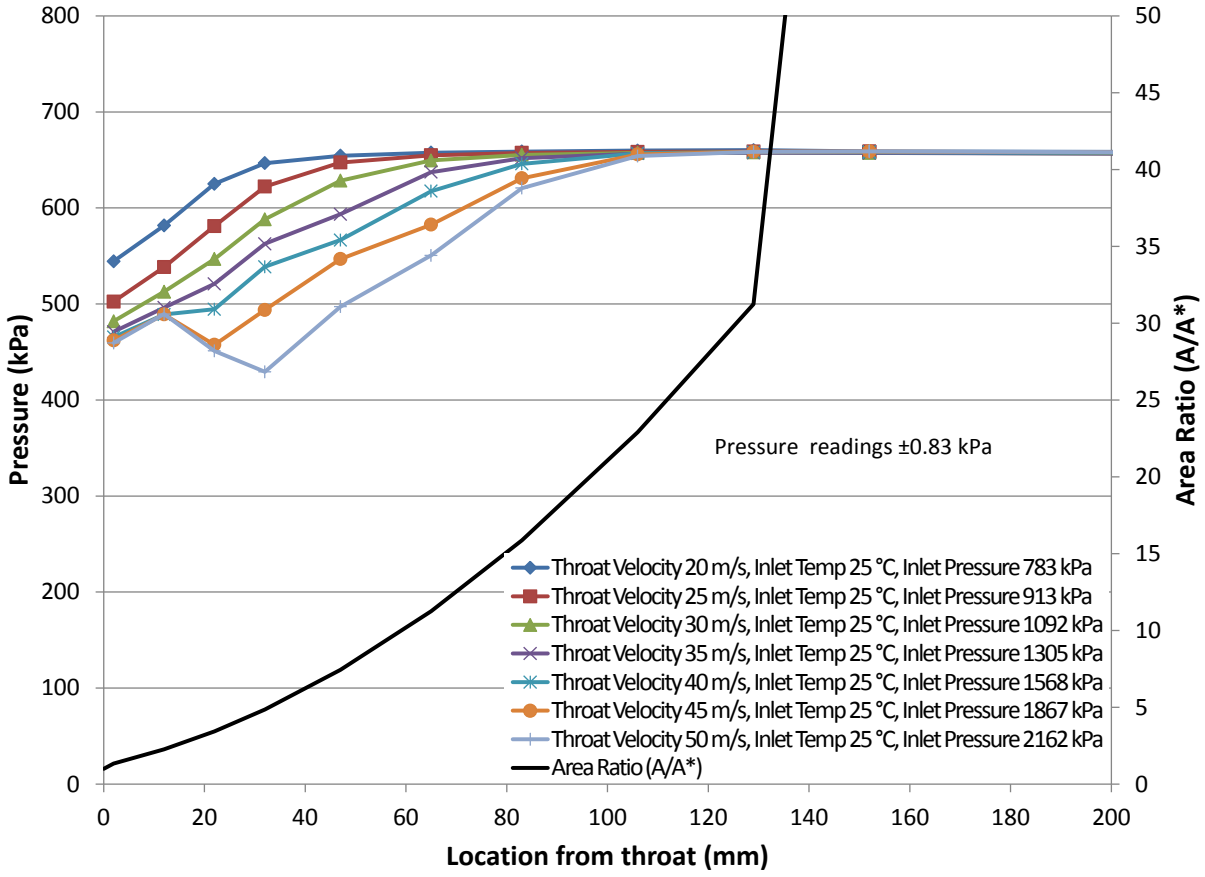

Figure 4.4: Nozzle C, Pressure vs Location

Also interesting is that for the first three taps, the pressures for a velocity of 50 m/s are approximately the same as for a velocity of 45 m/s. The increase in mass flow doesn't change the initial shape of the pressure profile, merely extends it further down the nozzle

Examining Nozzle D in Figure 4.5, we see somewhat similar behavior. The lowest pressure measured occurs not at the first pressure tap, but at the second, a distance of 22 mm from the throat. However, for the first pressure tap at 2 mm, the measured pressure for a velocity of 50 m/s is actually higher than for a velocity of 45 m/s.

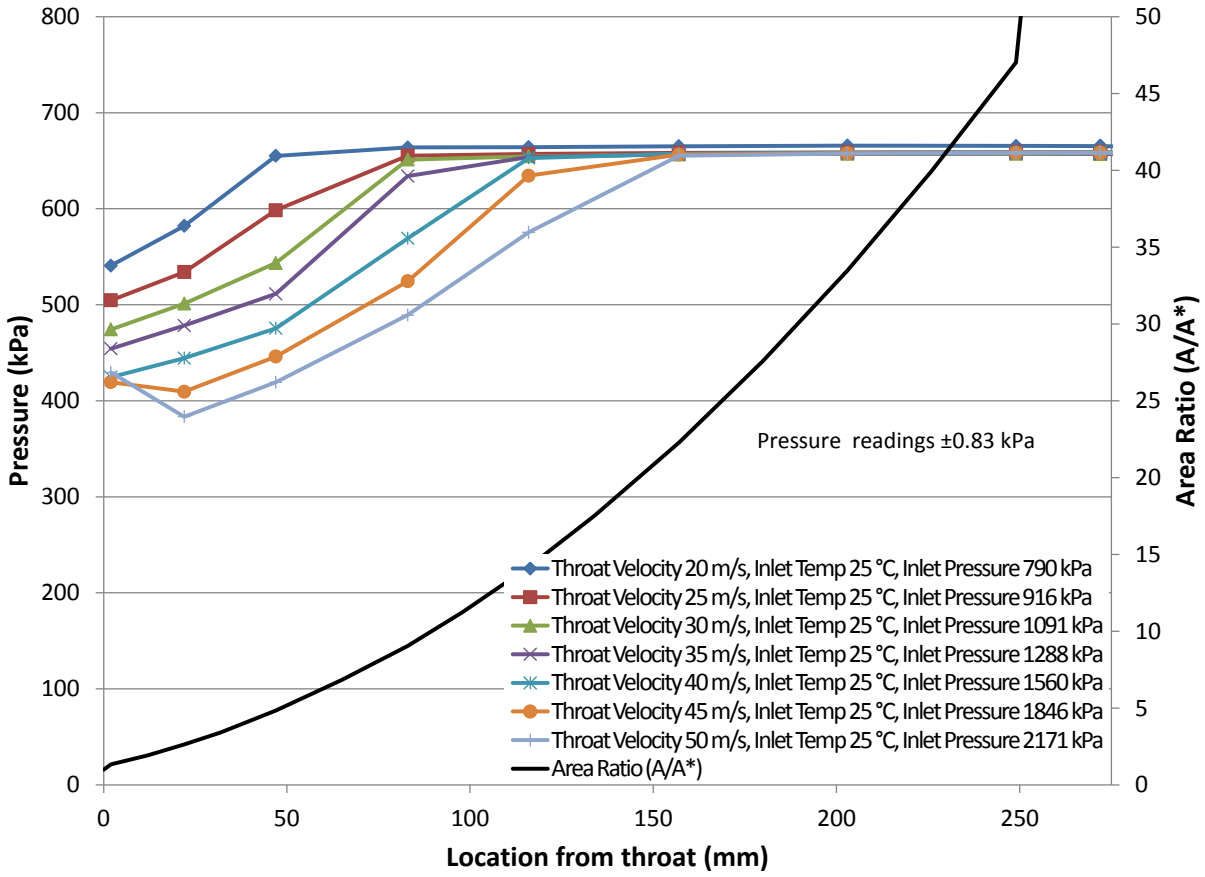

Figure 4.5: Nozzle D, Pressure vs Location

If we compare all of the nozzles for a velocity of 50 m/s as in Figure 4.6, we can make several observations. First, Nozzle D, with a longer length and slower area growth, has both the lowest measured pressure and the slowest rise back to the outlet pressure. Second, Nozzle B and Nozzle C, both having geometry including the IFM, have similar profiles, only differing significantly between 22 mm to 65 mm. Third, Nozzle A, though it has the same expansion angle as Nozzle B and Nozzle C, shows no measured decrease in pressure with increasing area after the first tap. Finally, all three 1.5° expansion nozzles all come back to the outlet pressure by 106 mm , compared with Nozzle D at 157 mm.

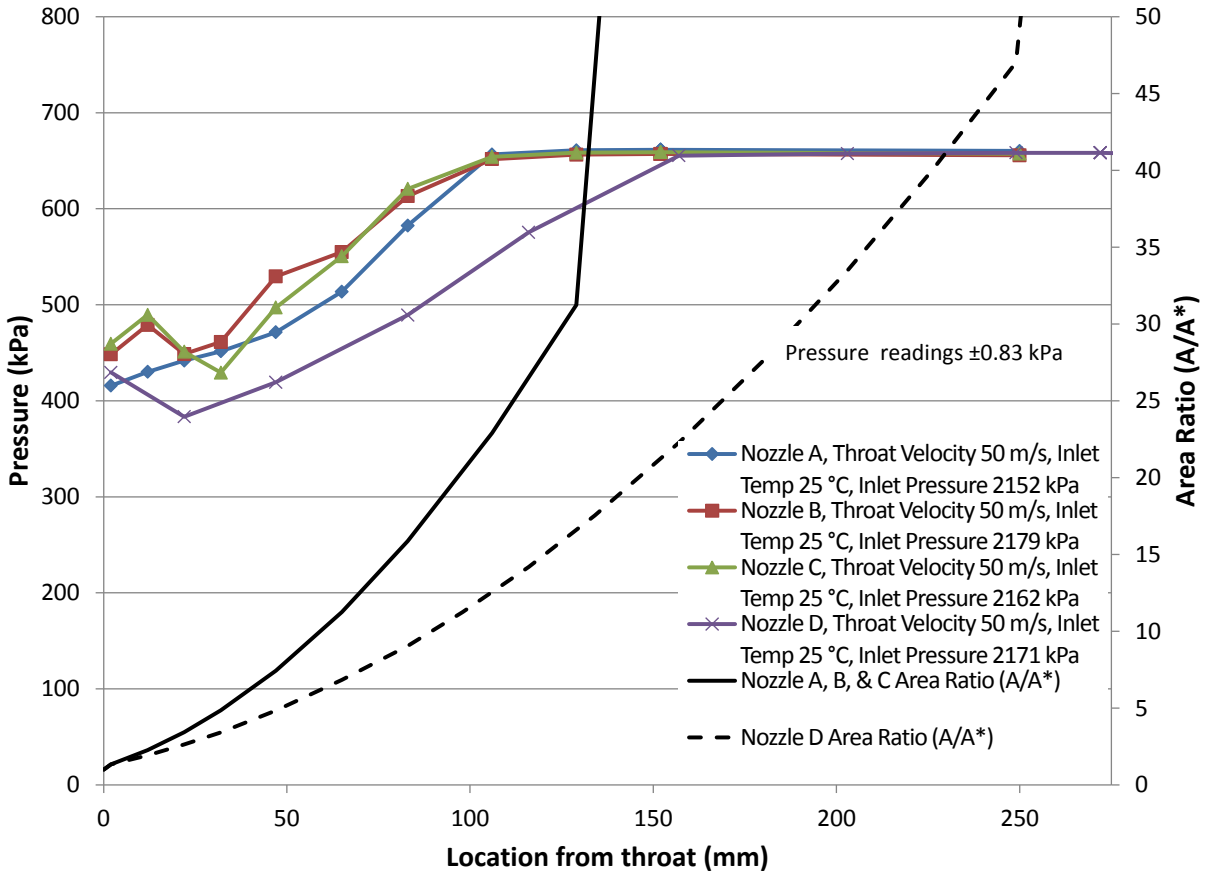

Figure 4.6: Pressure vs Location, All Nozzles at 50 m/s

4.3 Temperature Profile

As our models only make use of the inlet temperature, we will not delve much into the temperature profiles of the tested nozzles except to note several trends. As stated in Chapter 2, temperatures were measured using K-type ungrounded thermocouple probes located in taps at various locations down the length of the nozzle, with 0.66 mm of aluminum between the probe sheaths and the flow. Though the exterior of the nozzle is insulated, it is likely that some conduction is occurring along the length of the nozzle. However, it is interesting to look at the temperatures measured as they show a substantial drop below the inlet temperature, followed by a rise back up. This is illustrated for Nozzle A in Figure 4.7.

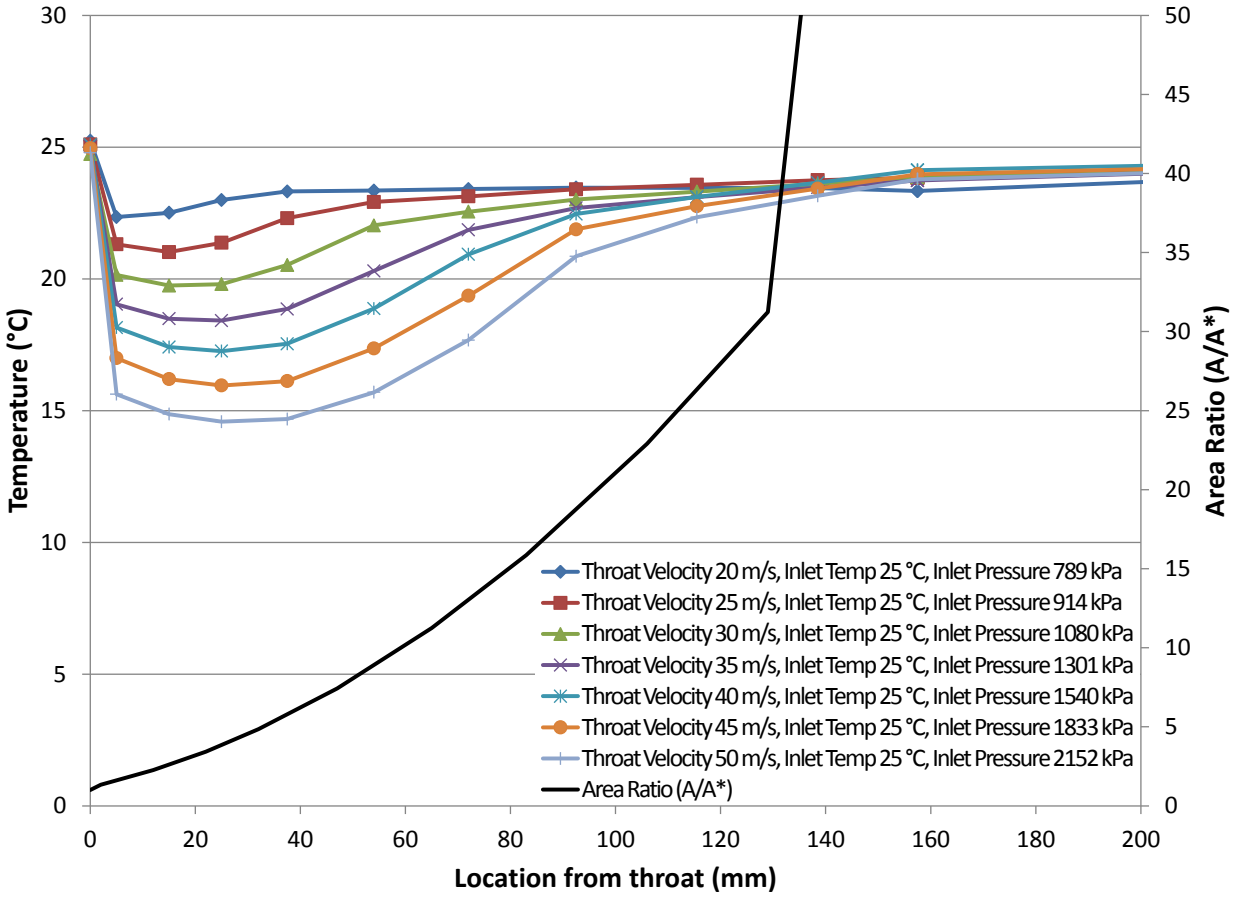

Figure 4.7: Nozzle A: Temperature vs Location

Note that though a measured temperature is indicated at the throat, this measurement takes place upstream of the throat and is simply shown at $z = 0$ for the sake of a compact graph. As the piping and nozzle inlet are well insulated, it is reasonable to expect that this temperature persists while the fluid is liquid up to the throat. Following the throat, the temperature declines rapidly to the first temperature tap and continues to decrease at a slower pace as we proceed down the nozzle. The temperature hits a minimum and gradually begins to increase at an accelerating rate until it reaches a temperature somewhat below the inlet temperature. As with the pressure profile, increased throat velocities yield lower temperatures.

The differences in the overall behavior of the temperature profiles of the nozzles are somewhat unremarkable when compared with the differences in the pressure profiles. As such,

we will simply compare all nozzles' temperature profiles at the highest velocity of 50 m/s, shown in Figure 4.8.

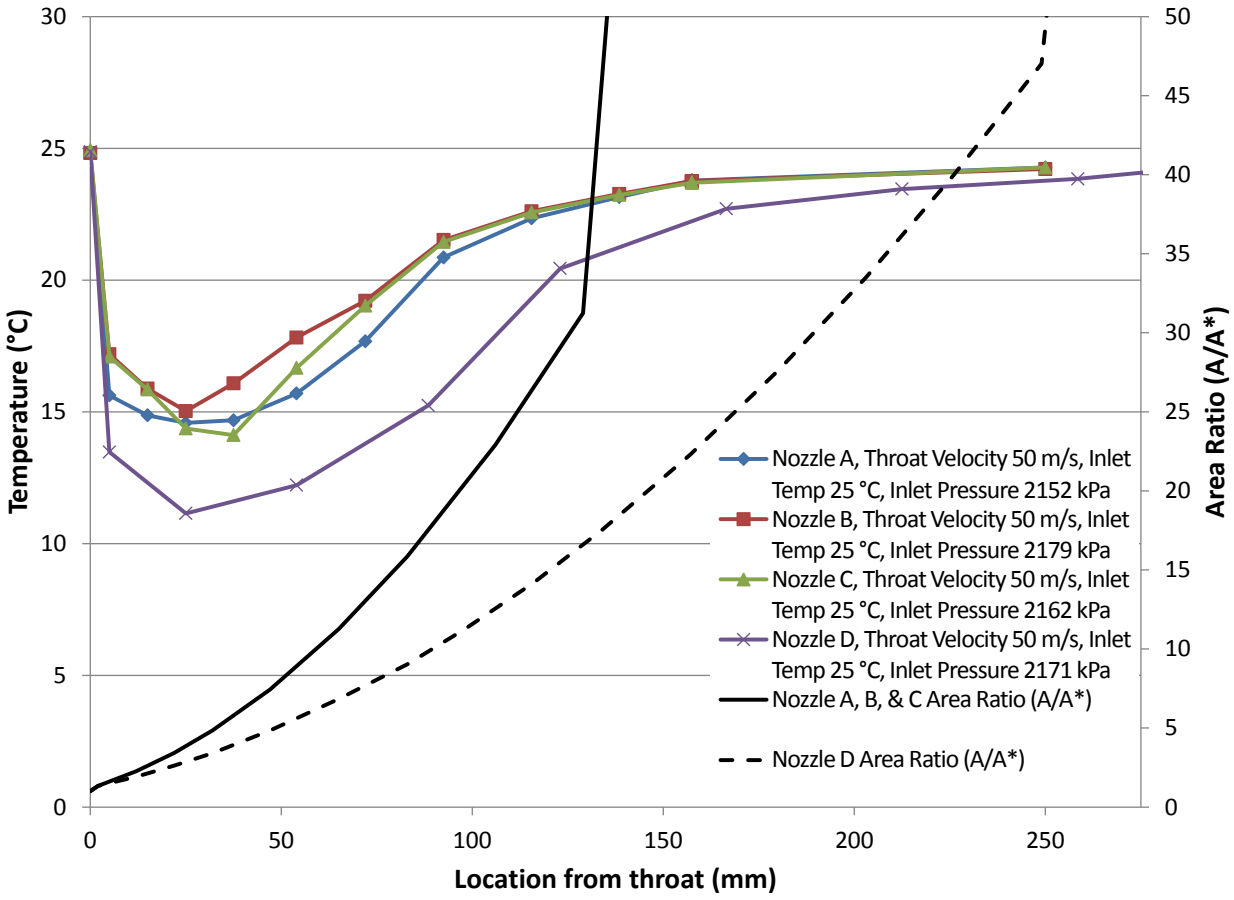

Figure 4.8: Temperature vs Location, All Nozzles at 50 m/s

As with the plots of pressure profiles for a velocity of 50 m/s, we can observe several trends. Nozzle D, with the longest length and slowest area growth, sees both the largest drop in temperature and the longest persistence until the temperature comes back up. Nozzles A, B, and C are very similar, but Nozzle A without the IFM has the smoothest transition between temperature measurements. All nozzles experience the greatest drop in temperature by the first temperature tap at 5 mm after the throat, yet all also have their minimum temperature somewhere after this point.

4.4: Pressure Compared with Temperature

As both models we are applying to our data assume thermal equilibrium, it follows that we should compare measured pressure to measured temperature. Thermal equilibrium would require that a change in pressure correspond with a change in temperature. Figure 4.9, showing pressure and temperature vs location for Nozzle A shows that is not exactly the case.

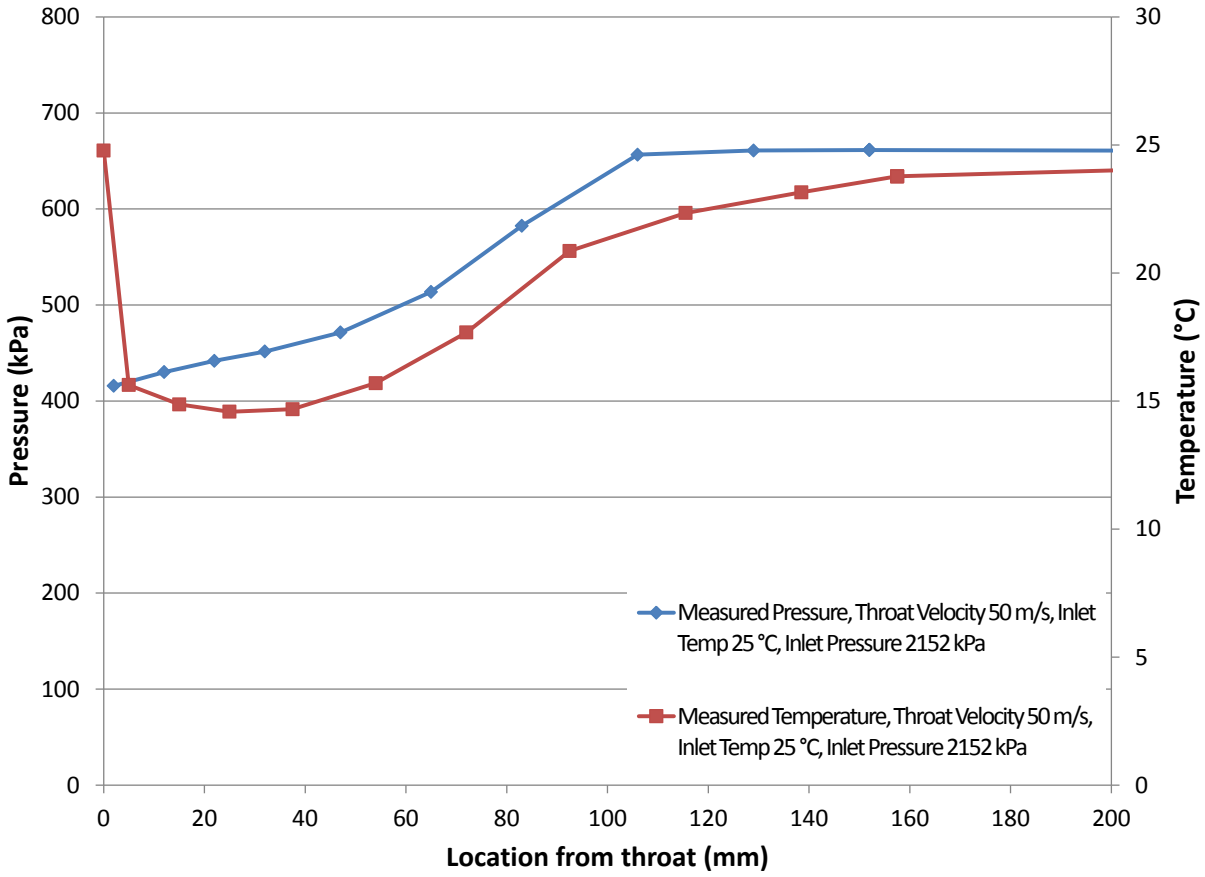

Figure 4.9: Nozzle A, Pressure and Temperature vs Location at 50 m/s

Both pressure and temperature show drops at the first tap. But while pressure reaches its minimum at the first tap, temperature does not reach its minimum until approximately 30 mm after the throat. Following that, both pressure and temperature appear to follow each other.

Similar behavior can be seen for Nozzle B in Figure 4.10. Both pressure and temperature initially behave differently.

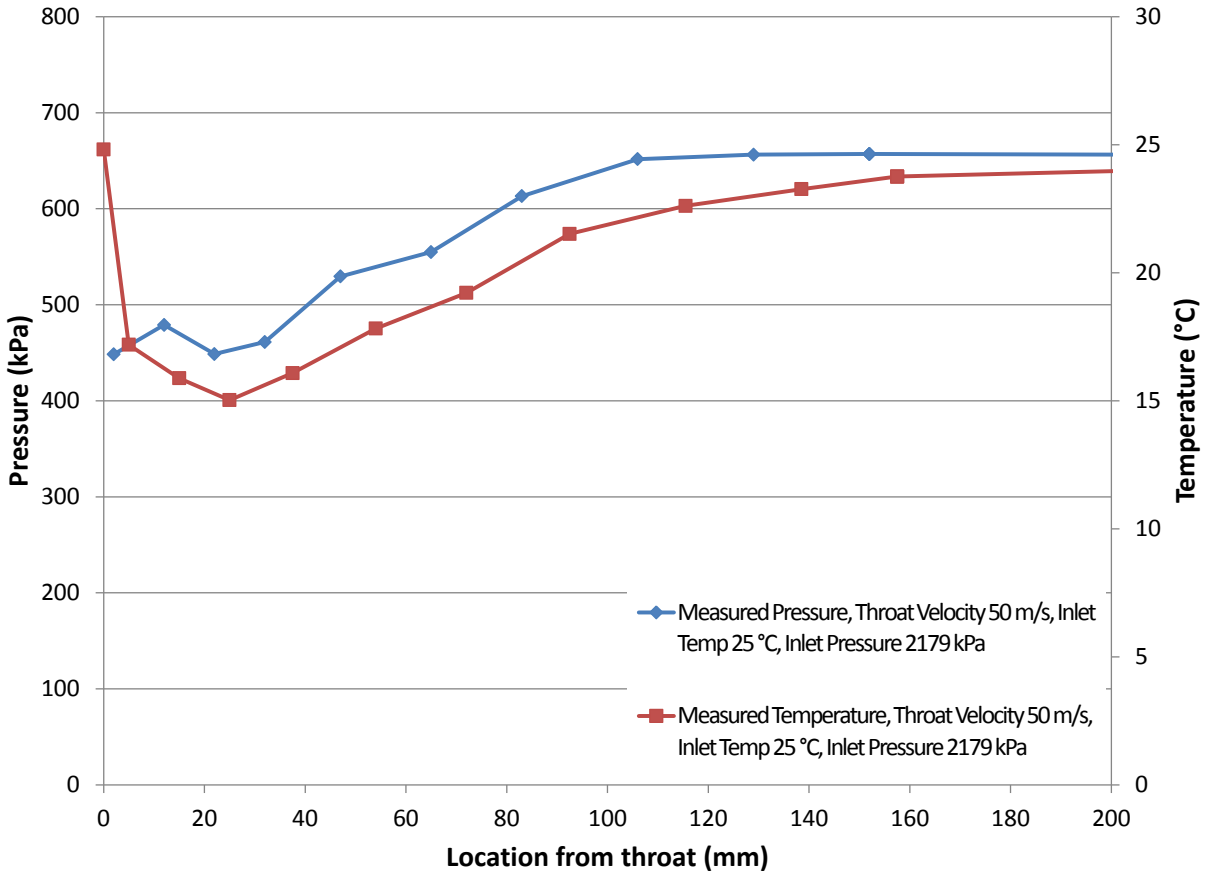

Figure 4.10: Nozzle B, Pressure and Temperature vs Location at 50 m/s

However, for Nozzle D, the difference in behavior between pressure and temperature is not as apparent. As seen in Figure 4.11, changes in pressure correspond well with changes in temperature, with a slight exception at approximately 123 mm after the throat. Both pressure and temperature drop the largest amounts by the first tap and then continue to track with each other after that. After 150 mm, pressure has reached roughly a constant value while temperature continues to slightly increase to its exit value, but overall they correspond well. The slow changes in temperature seen in the latter section of all nozzles may simply be due to thermal gradients in the aluminum nozzle due to heat flowing from the relatively warm end of the nozzle towards the colder throat region. Unfortunately, nothing prevents axial conduction in this manner.

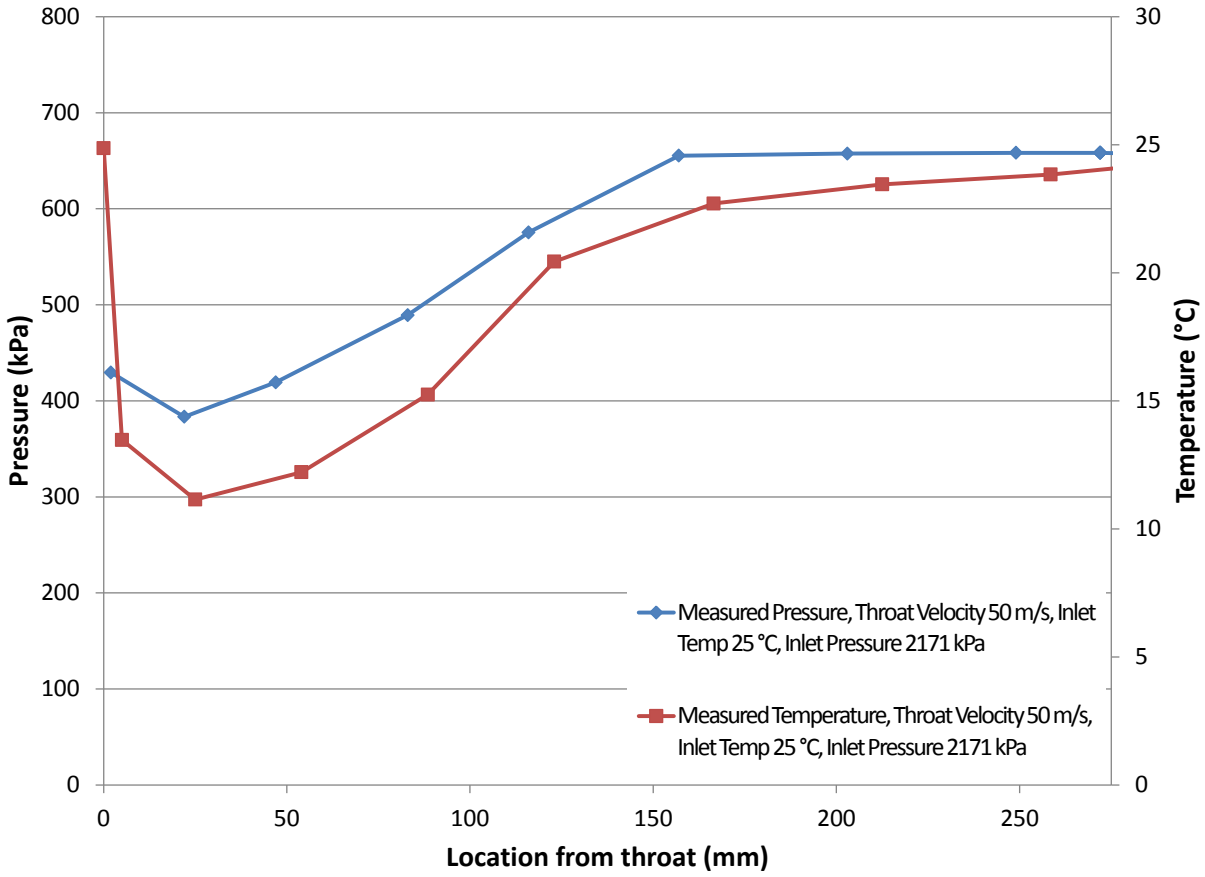

Figure 4.11: Nozzle D, Pressure and Temperature vs Location at 50 m/s

The differences seen in the initial sections of Nozzles A, B, and C seems to indicate that the assumption of thermal equilibrium may be flawed. As stated in Chapter 1, it is known that this assumption is not always valid, as appears to be the case. However, it is still useful to see what effects this assumption causes in our analysis.

One final thing to note is that the outlet pressures seen in these nozzles of approximately 650 kPa to 670 kPa correspond with a saturation pressure of about 25°C. As our measured exiting temperatures are in the range of 23°C to 24°C, this would indicate that the fluid is leaving the nozzle in a subcooled state. However, it may be possible that vapor bubbles are persisting out of the nozzle.

Chapter 5 - Data Reduction and Model Implementation

Before we can apply our models to our experimental data, we must first shape the data into a form that fits our integral form of our equations. Conservation of momentum equations for both the HEM and separated flow model developed in Chapter 3 both require knowledge of the pressure as a function of location z. We currently have the pressure at intermittent locations down the nozzle. A curve fit allows us to find the pressure in between our pressure tap locations. But the conditions in the throat must first be established in order to create a curve fit from the throat to the exit. Following the creation of the curve fit, we discuss how the models are applied to the experimental data and solved.

5.1 Throat Conditions

We begin by assuming that the fluid is fully liquid up to the throat. Assuming that the fluid has the same temperature at the throat as it does upstream, conservation of mass gives us that the throat velocity is given by

$$V_t = \frac{\dot{m}}{\rho_t A_t} \tag{5.1}$$

where $\dot{m}$ is measured, ρ_t is the saturated liquid density for $T_t = T_{inlet}$, and A_t is calculated from the measured diameter of the throat. This velocity can then be applied to Bernoulli's Principle with losses for horizontal flow:

$$p_{inlet} + \frac{1}{2}\rho_{inlet}V_{inlet}^2 = p_t + \frac{1}{2}\rho_t V_t^2 + H \tag{5.2}$$

Here, p_{inlet} is measured, $\rho_{inlet} = \rho_{sub}(T_{inlet}, p_{inlet})$, V_{inlet} is calculated through conservation of mass, and H is our head loss. Rearranging [5.2] to solve for the throat pressure we find

$$p_t = p_{inlet} + \frac{1}{2}(\rho_{inlet}V_{inlet}^2 - \rho_t V_t^2) - H \quad [5.3]$$

which shows that $p_t < p_{inlet}$. Note also, that for any reasonable value of head loss ($H \geq 0$), p_t can only be lower. Rather than calculating the value of head loss, we will simply set $H = 0$ and calculate the throat pressure from

$$p_t = p_{inlet} + \frac{1}{2}(\rho_{inlet}V_{inlet}^2 - \rho_t V_t^2) \quad [5.4]$$

while recognizing that p_t in actuality is less than this calculated value.

We must also look at what properties this liquid must have at this calculated pressure. If we calculate the saturated pressure for the measured inlet temperature, we find that the calculated throat pressure is less than the saturated pressure. As seen in Table 5.1, this holds true for all throat velocities in Nozzle A.

Table 5.1: Nozzle A, Calculated Throat Pressure Compared with Saturation Pressure

V_t (m/s)	p_t (kPa)	$p_{sat}(T_{inlet})$ (kPa)	T_{inlet} (°C)
20	539	670	25.2
25	529	667	25.1
30	529	660	24.7
35	552	666	25.0
40	575	667	25.1
45	590	665	25.0
50	606	661	24.8

That $p_t < p_{sat}(T_{inlet})$ holds true for all other nozzles at all throat velocities as well. As stated above, including head loss will only cause p_t to be lower. The physical meaning of this condition is that the liquid is under tension in a metastable state. The pressure has dropped rapidly enough that the liquid is existing in a state below its saturation pressure for its temperature. This metastable state is a non-equilibrium condition and likely affects the validity

of the models chosen. Often, this state is referred to as having a negative equivalent equilibrium quality, but for our models we will simply set the quality at the throat, x, to be 0.

Quality, pressure, velocity, and temperature at the throat are the only properties necessary for us to apply our model. We cannot find the enthalpy at the throat with normal property references such as REFPROP. Instead, we can find the throat enthalpy by use of the subcooled inlet enthalpy calculated through REFPROP from T_{inlet} and p_{inlet} and an energy balance from the inlet to the throat.

5.2 Pressure Curve Fit

Due to the use of the integral form of the momentum equation, it is necessary to know, or at least reasonably approximately, how pressure varies as a function of position. To that end, we apply a curve fit to the data.

From the first pressure tap to the end of the nozzle, a piecewise-continuous, cubic spline fit is used. The ends of the spline fit are natural, meaning that $p"(z_1) = p"(z_{end}) = 0$, in order to lessen oscillations within the curve fit. However, for the first section from the throat to the first tap, a linear fit is used, as a spline fit in this section would cause unrealistic fitted pressures due to the rapid change in pressures that occurs for most nozzles in this section. The curve fit for Nozzle A is shown in Figure 5.1. The curve fit appears to match the data for Nozzle A well. As we don't know the actual shape of the pressure profile between the throat and the first tap, the linear fit in this section allows us to avoid the large dip that continuing the spline fit would cause. The same can be seen in the curve fit for Nozzle B in Figure 5.2. The curve fit is able to match all pressures after the first tap. Though it is not known exactly how the pressure changes between the latter taps, it is reasonable to assume gradual transitions between pressure measurements.

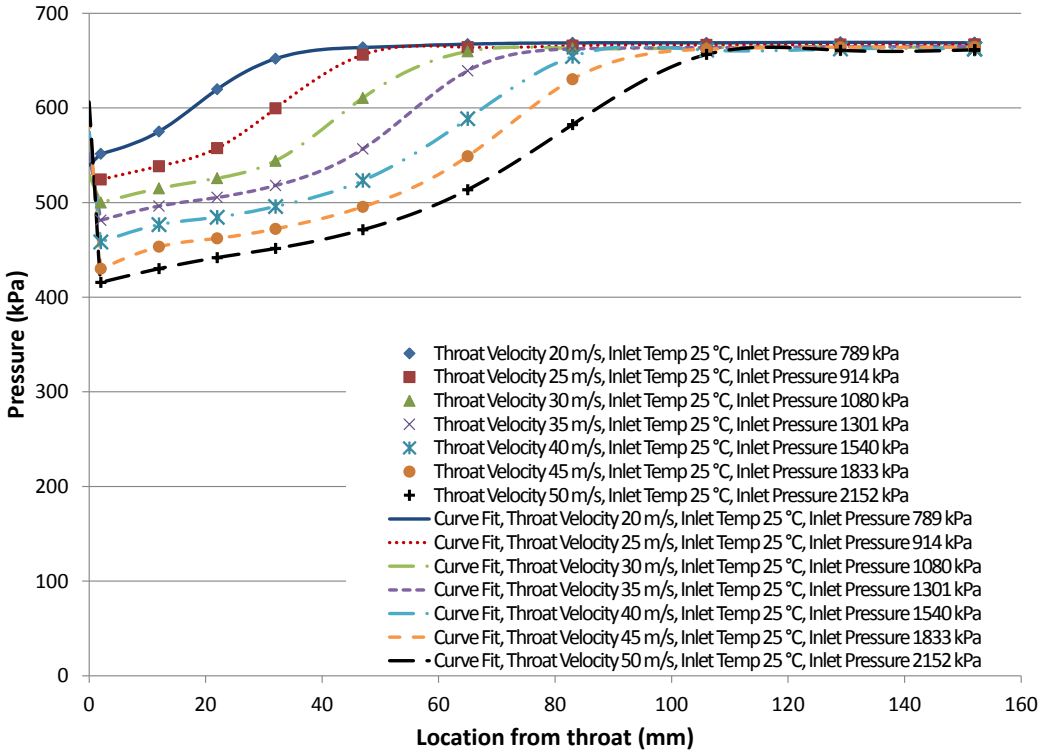

Figure 5.1: Nozzle A, Pressure Curve Fit

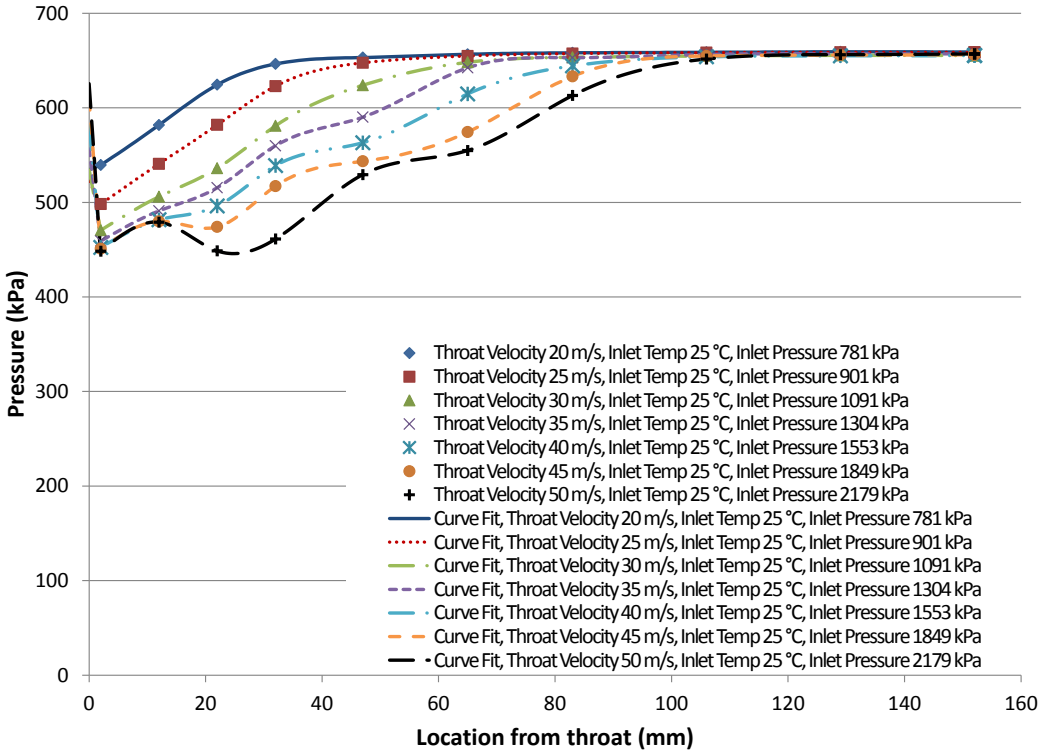

Figure 5.2: Nozzle B, Pressure Curve Fit

Looking at the curve fit for Nozzle C in Figure 5.3, we see the curve fit is even able to handle the large dip that occurs from the second to fourth pressure taps for a throat velocity of 50 m/s.

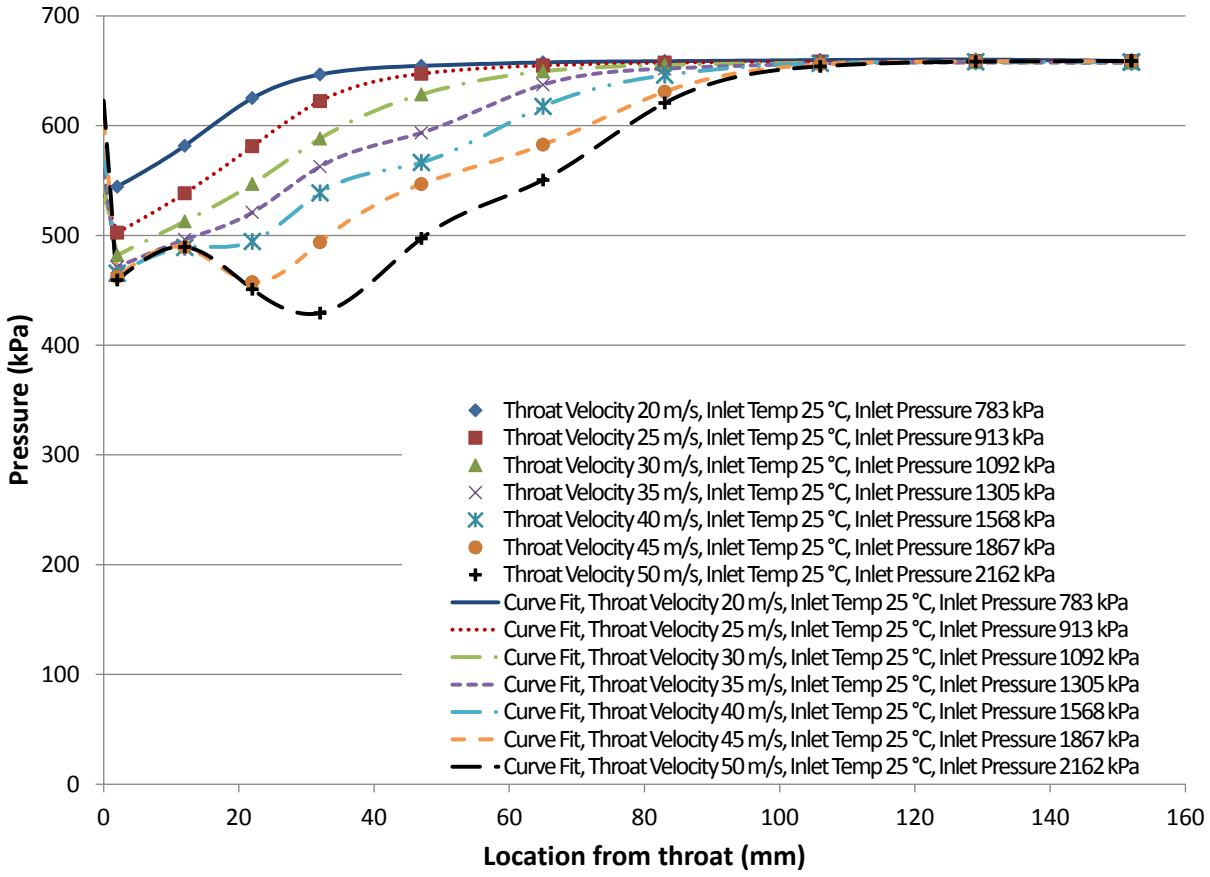

Figure 5.3: Nozzle C, Pressure Curve Fit

The curve fit matches similarly well for Nozzle D. For all nozzles, there are some oscillations that occur in the latter sections of the nozzle. Mostly this occurs where the pressure is essentially constant. This oscillation does not seem to affect results.

5.3 Model Implementation

The models are implemented and applied to the experimental data in Microsoft Excel. Excel's Solver add-in is used to vary quality, liquid velocity, and a friction term F_τ given by

$$F_{\tau,i\to i+1} = 2\pi \int_{i}^{i+1} \tau(z)\, r(z) dz \qquad [5.5]$$

equivalent to the total force due to wall shear over the interval i to $i+1$, where i is the ith pressure tap. These variables are iterated, with the equations of Chapter 3 simultaneously solved, until all equations over each interval between adjacent pressure taps are satisfied. When quality is forced to zero by the solver and the equations cannot be satisfied, a fourth variable of temperature is iterated as well to allow for subcooled conditions. Properties of density and specific enthalpy are evaluated using REFPROP version 9.1 at the saturated conditions using the measured pressures for most cases or the subcooled case using both the measured pressures and iterated temperatures when necessary (Lemmon, Huber et al. 2013).

Properties such as sound speed are also calculated and used for analysis, though are not required to satisfy the conservation equations. They are instead used in the calculation of the two-phase speed of sound calculation of [1.2] for the HEM case in order to find the local Mach number at each tap location.

Chapter 6 - Analysis Results

6.1 Quality, Void Fraction, and Mach Number

We begin by looking at the quality vs position for all throat velocities of Nozzle A in Figure 6.1.

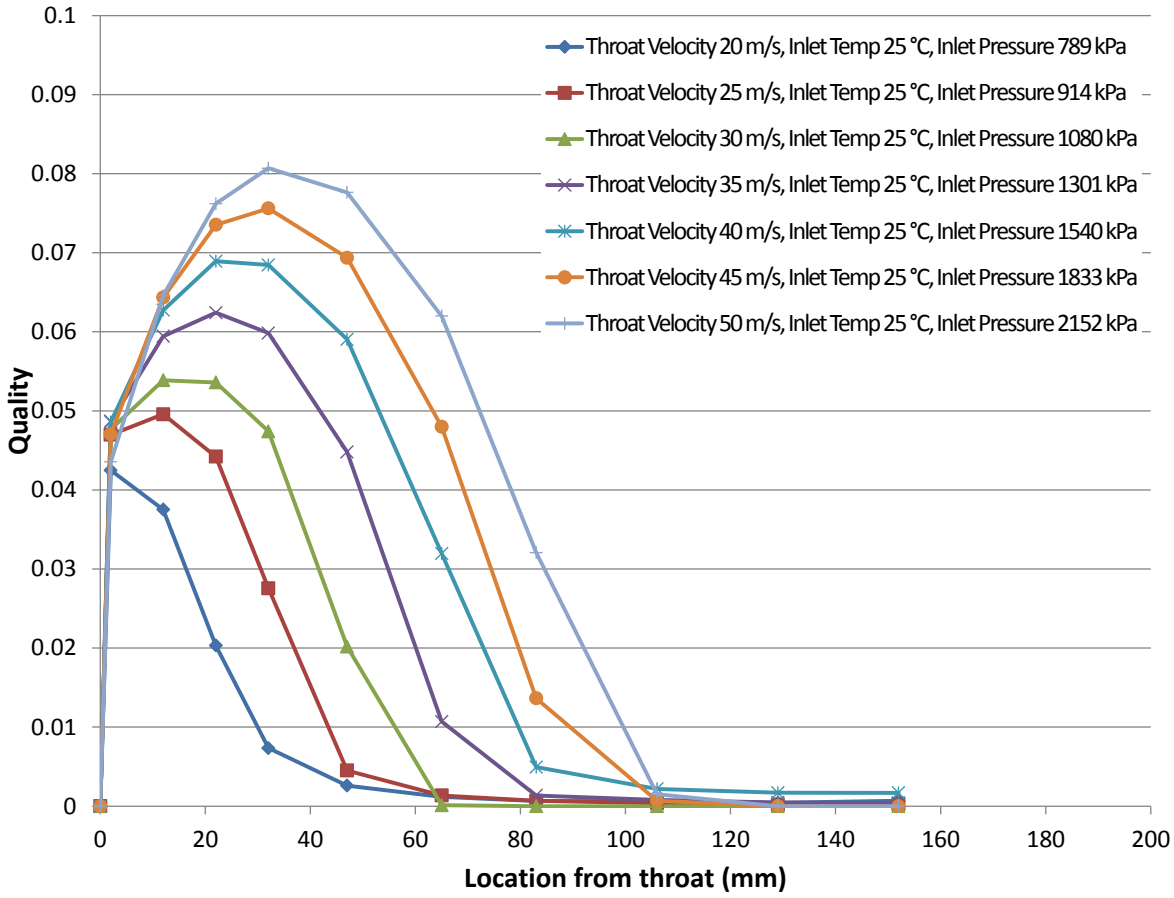

Figure 6.1: Nozzle A, HEM, Quality vs Location

We note that quality increases with throat velocity. Qualities also reach their maximum further down the nozzle as the throat velocity is increased. An increase in velocity also corresponds to an increase in the length at which the quality returns to zero or near zero. Interestingly, if we refer to the pressures of Nozzle A as shown in Figure 4.2, we see that the maximum quality does not occur at the point of minimum pressure, but in a location where pressure is already

increasing. If we observe nozzle A again, but assuming separated flow with $n = 1/3$, we see the same trend, but with slightly higher qualities. This is shown in Figure 6.2.

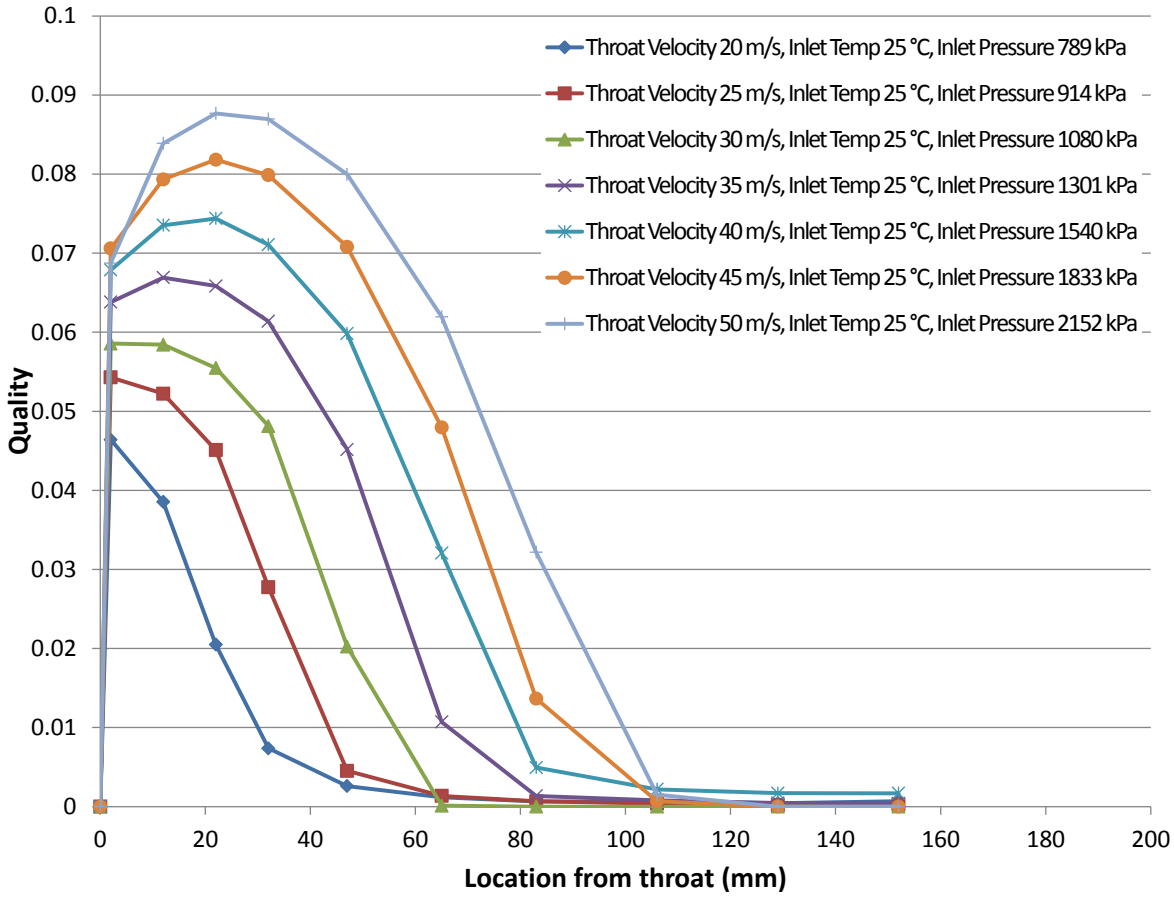

Figure 6.2: Nozzle A, Separated Flow with n=1/3, Quality vs Location

Comparing the qualities for all models of Nozzle A for a throat velocity of 50 m/s in Figure 6.3, we see the same overall behavior. Interestingly, the higher the quality predicted, the closer to the throat the maximum quality occurs. After a certain point, all models' predictions lie atop each other. The case assuming $n = 1/3$ predicts the highest quality. This trend holds true for the other nozzles as well. As this value of n is designed to maximize the kinetic energy, a higher quality might be expected. The same behavior is seen in all other nozzles when comparing between models.

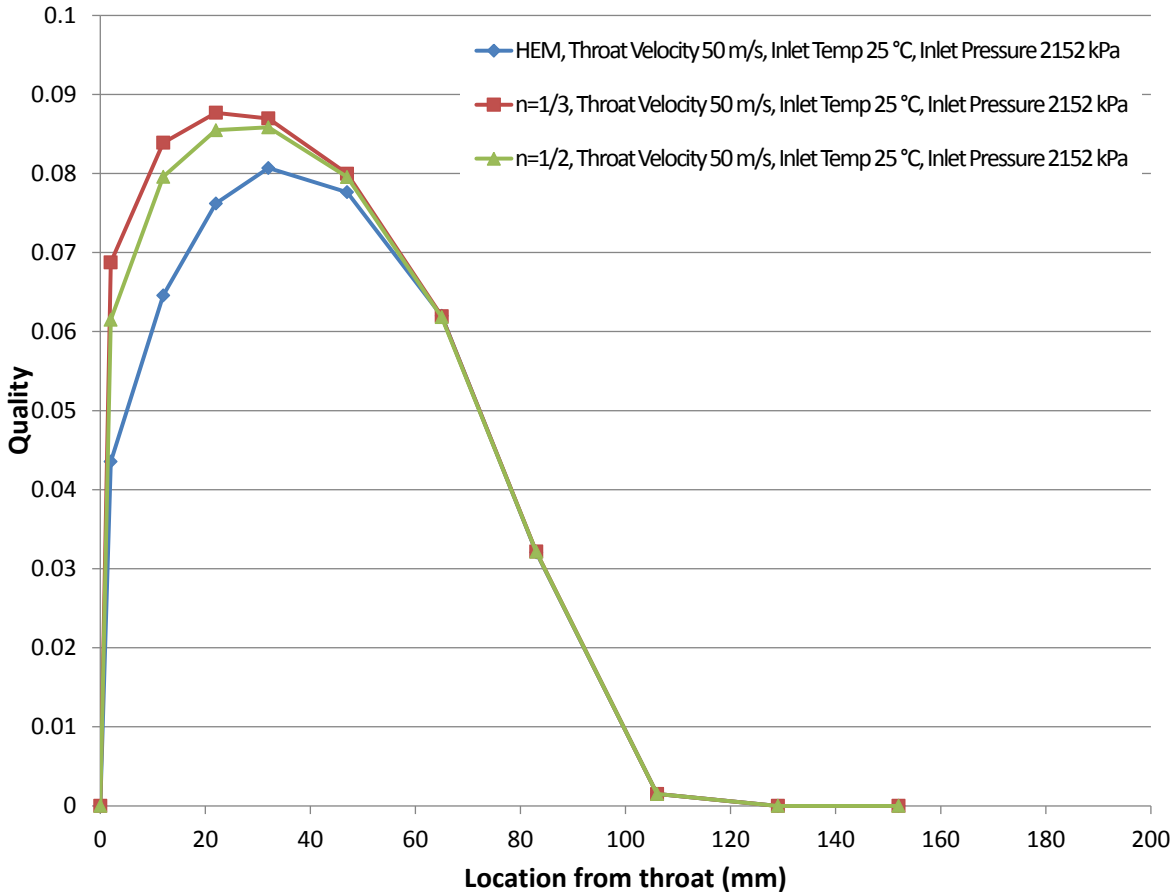

Figure 6.3: Nozzle A, All Models, Quality vs Location at 50 m/s

Comparing between nozzles for the HEM at 50 m/s in , we do not see significant differences in the predicted quality between Nozzles A, B, and C. The quality for Nozzle A seems smoother, but the values are approximately the same. Nozzle D with its slower area growth shows both the highest quality and the longest distance over which a significant quality occurs.

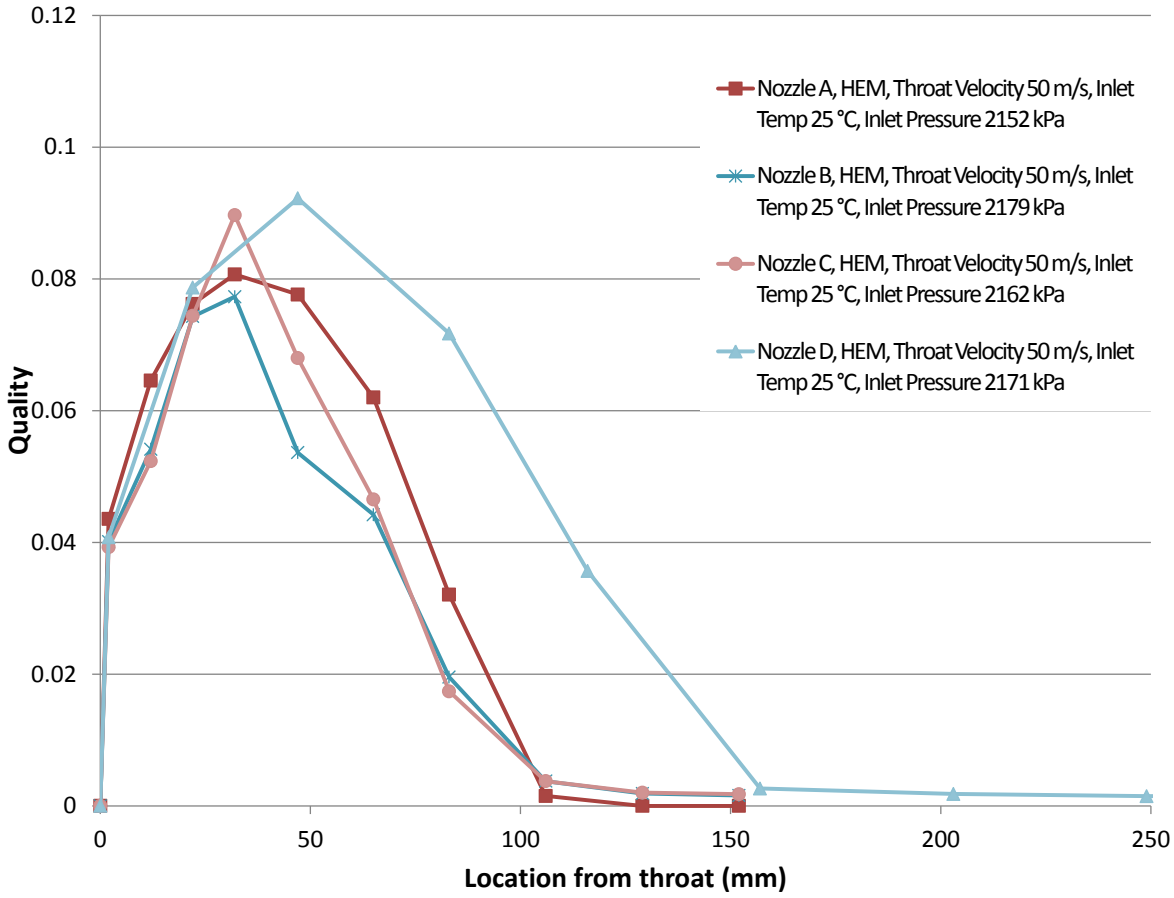

Figure 6.4: All Nozzles, HEM, Quality vs Location

Now we turn our attention to the predicted Mach number. Note again that our calculation of Mach number of [1.3] is only valid for the HEM, as our two-phase speed of sound calculated by [1.2] is only valid for the HEM. If we observe the Mach numbers at all velocities for Nozzle A in Figure 6.5, we see that the maximum value is predicted near the throat, with increasing throat velocity yielding increased peak Mach number and distance down the nozzle until the Mach number is practically zero. Of note is that the HEM predicts that even for a throat velocity of 20 m/s the flow is going sonic, at least for the first pressure tap. If we observe the pressures for Nozzle A in Figure 4.2, it would seem as though Mach number corresponds to pressure, though we will soon find that this is not exactly the case.

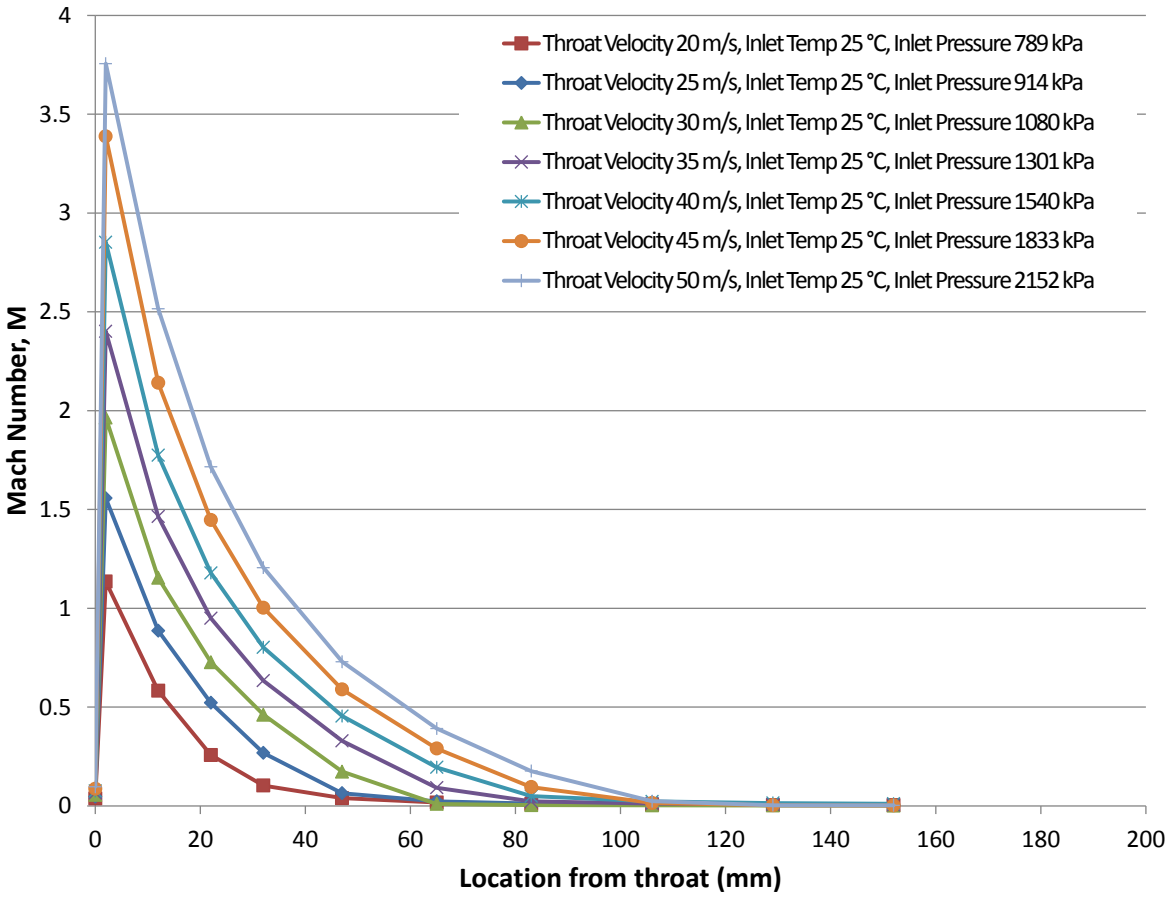

Figure 6.5: Nozzle A, Mach Number vs Location

If we now observe the Mach number for Nozzle B in Figure 6.6, very little is different. The main difference is that lower maximum Mach numbers are predicted for Nozzle B when compared with Nozzle A. Other than that, the same trend hold true with regards to increasing velocity yielding increased Mach number. If we compare the pressures of Nozzle B in Figure 4.3 to the Mach numbers of Figure 6.6, we see that the point of lowest pressure does not correspond with the highest Mach number. This is in contrast to single-phase sonic flow, in which we would expect the lowest pressure to correspond with the highest Mach number, showing again one of the unique aspects of sonic, two-phase flow.

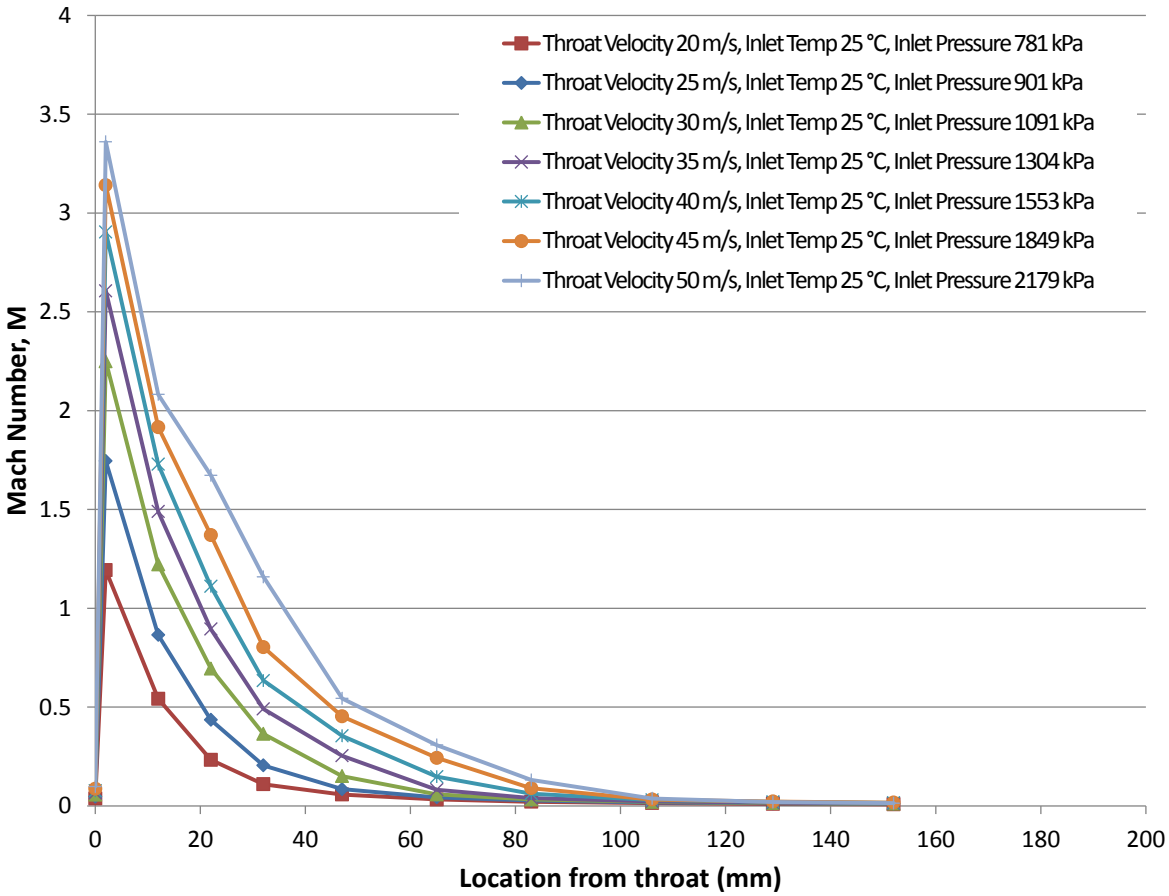

Figure 6.6: Nozzle B, Mach Number vs Location

However, Mach number does correspond with several important variables in our nozzles. As can be seen for Nozzle A with a throat velocity of 50 m/s in Figure 6.7, a Mach number of 1 corresponds to the point of maximum quality and maximum void fraction. The point of maximum quality and void fraction is the point at which we transition back to subsonic flow. The same holds true for the rest of the nozzles, as can be seen for Nozzle B in Figure 6.8.

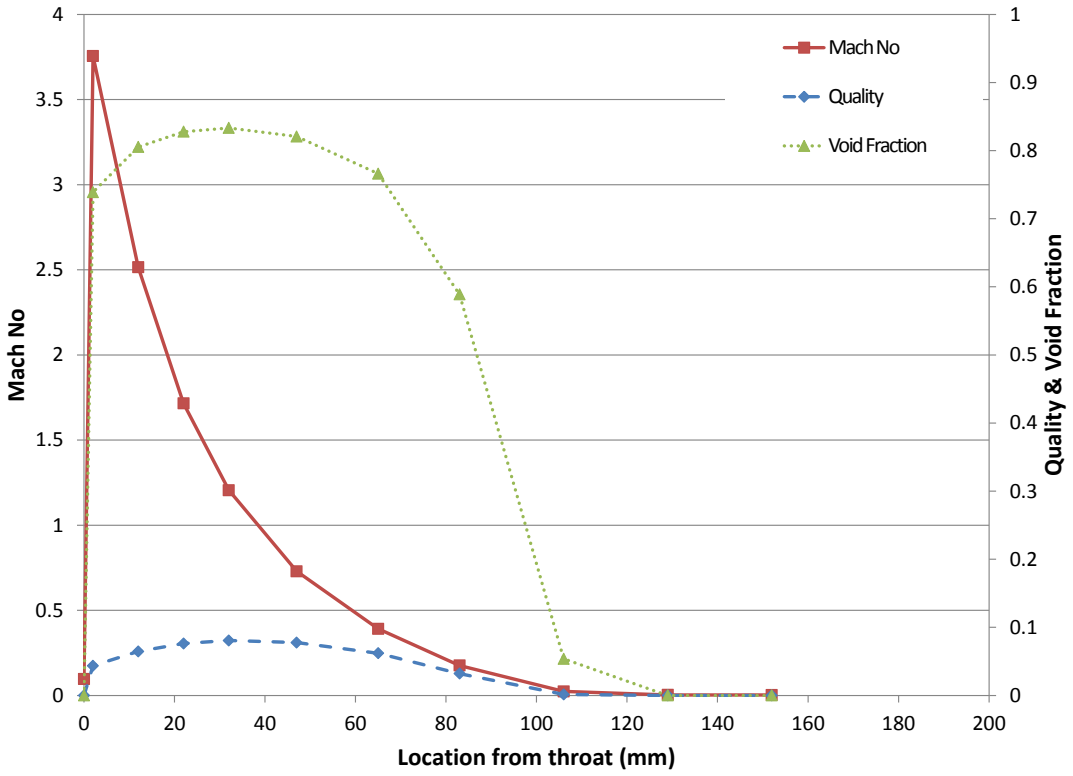

Figure 6.7: Nozzle A, Mach No, Quality, and Void Fraction vs Location at 50 m/s

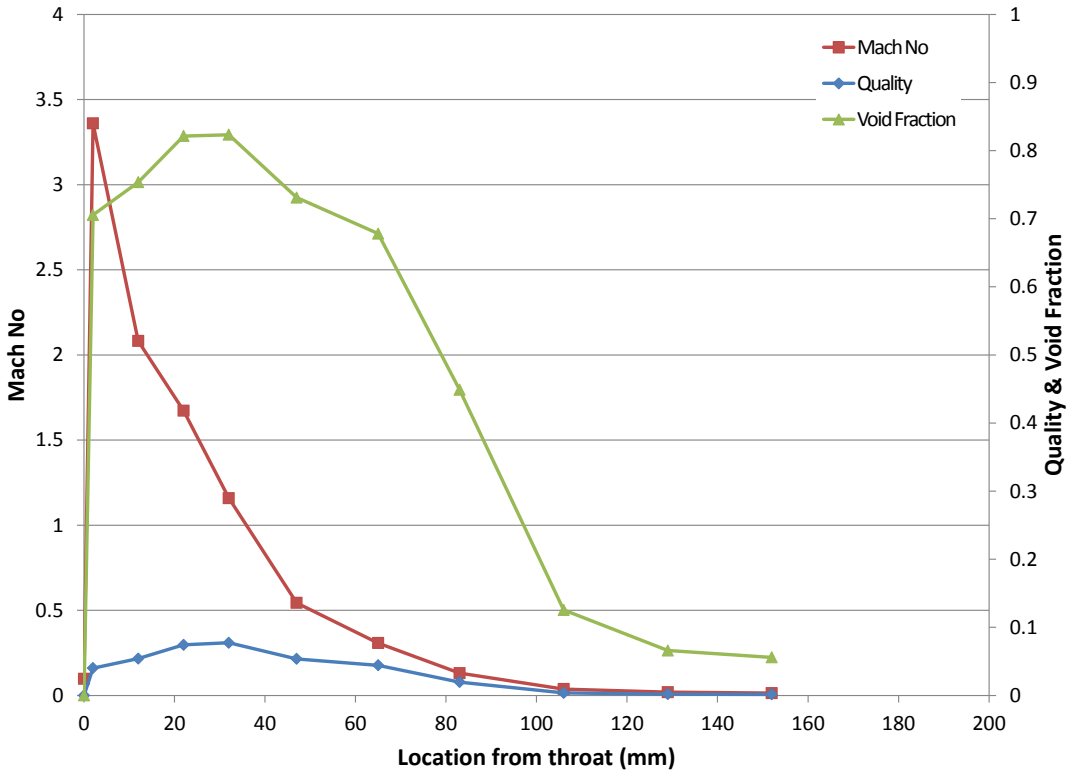

Figure 6.8: Nozzle B, Mach No, Quality, and Void Fraction vs Location at 50 m/s

The void fraction has increased such that the flow has been forced out of the sonic region. This can be seen most easily in Figure 6.9, in which we plot sound speed for R-134a and fluid velocities for all nozzles with a throat velocity of 50 m/s against void fraction. Note that this is the two-phase speed of sound at 20°C, simply chosen as a representative value of the fluid temperature down the length of the nozzle.

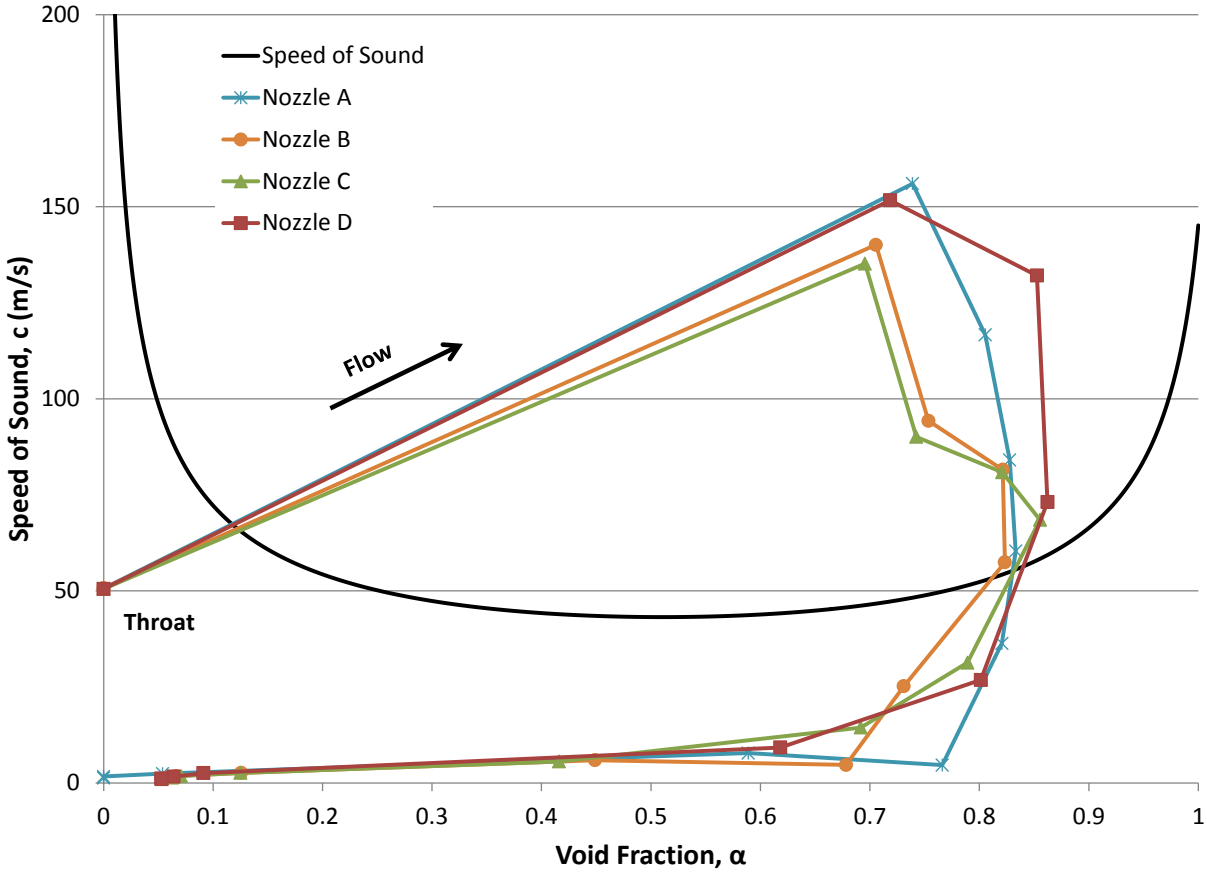

Figure 6.9: All Nozzles, Sound Speed and Fluid Velocities vs Void Fraction with Vt=50m/s

We can see the flow going sonic after the throat and before the first pressure tap. The flow reaches a peak velocity and then begins to slow down as void fraction increases. At a maximum value of void fraction, the flow transitions from sonic to subsonic. The velocity rapidly decreases with decreasing void fraction as the flow transitions back to liquid.

6.2 Shear Stress

The friction term $F_{\tau,i\to i+1}$ as described in [5.5] is from our conservation of momentum equation. If this term is divided by the surface area of the interval over which it was calculated, we get an average shear stress $\bar{\tau}_{i\to i+1}$ for that interval. Plotted, this shear stress shows both some expected and unexpected behaviors. For Nozzle A in Figure 6.10, we see shear stress plotted vs location for the HEM.

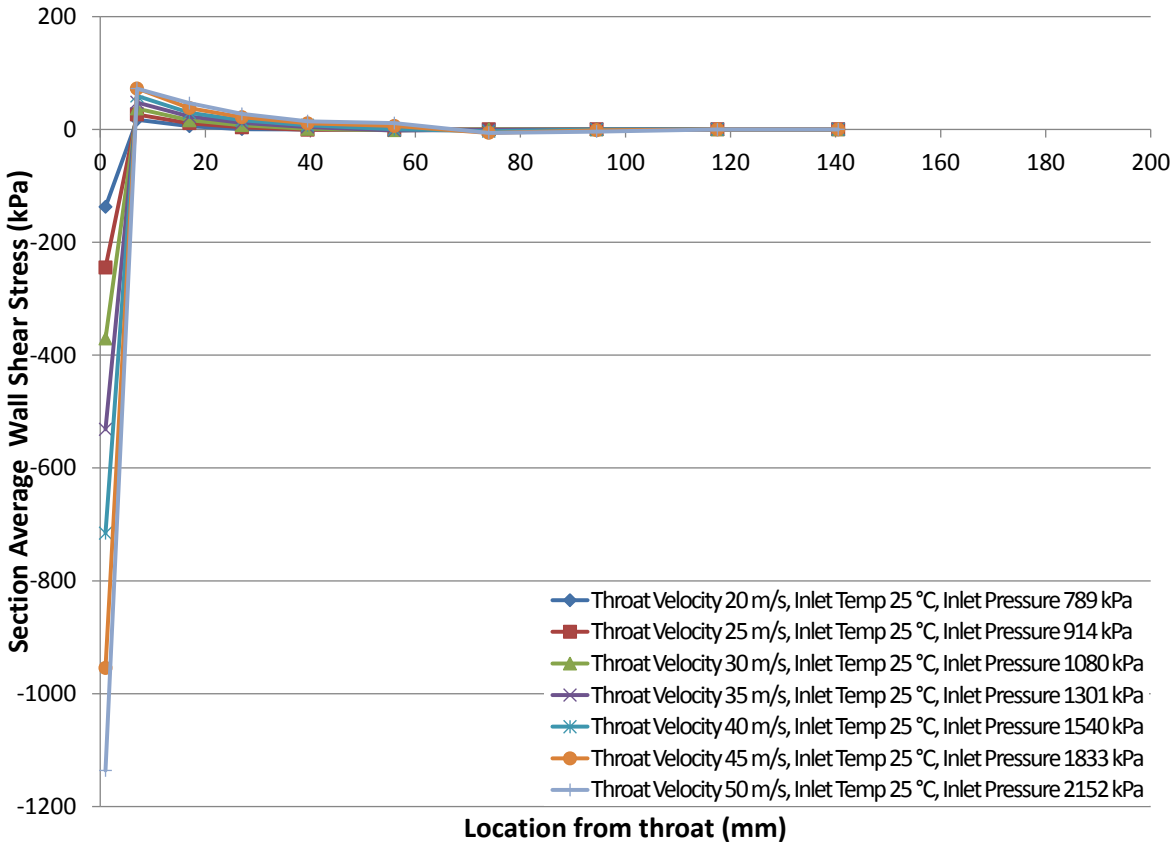

Figure 6.10: Nozzle A, Average Wall Shear Stress vs Location

What are immediately apparent are the very large negative values of average wall shear stress, whose magnitude increases with throat velocity. These negative values are seen in all nozzles with all models, though models with increased slip show smaller magnitudes. The reason for these negative values is unknown, though several theories exist. One thought is that due to the

non-equilibrium nature of our flow near the throat, the model is unable to accurately handle all forces in the momentum equation. Another idea is that the negative value, while not exactly accurate, indicates a force in the direction opposite our assumed flow direction due to a reversed flow in this section, as could occur with a vena contracta in the section immediately following the throat.

Ignoring the extreme negative shear values, we change the scale of our plot and look at shear values vs location in Figure 6.11 for Nozzle A.

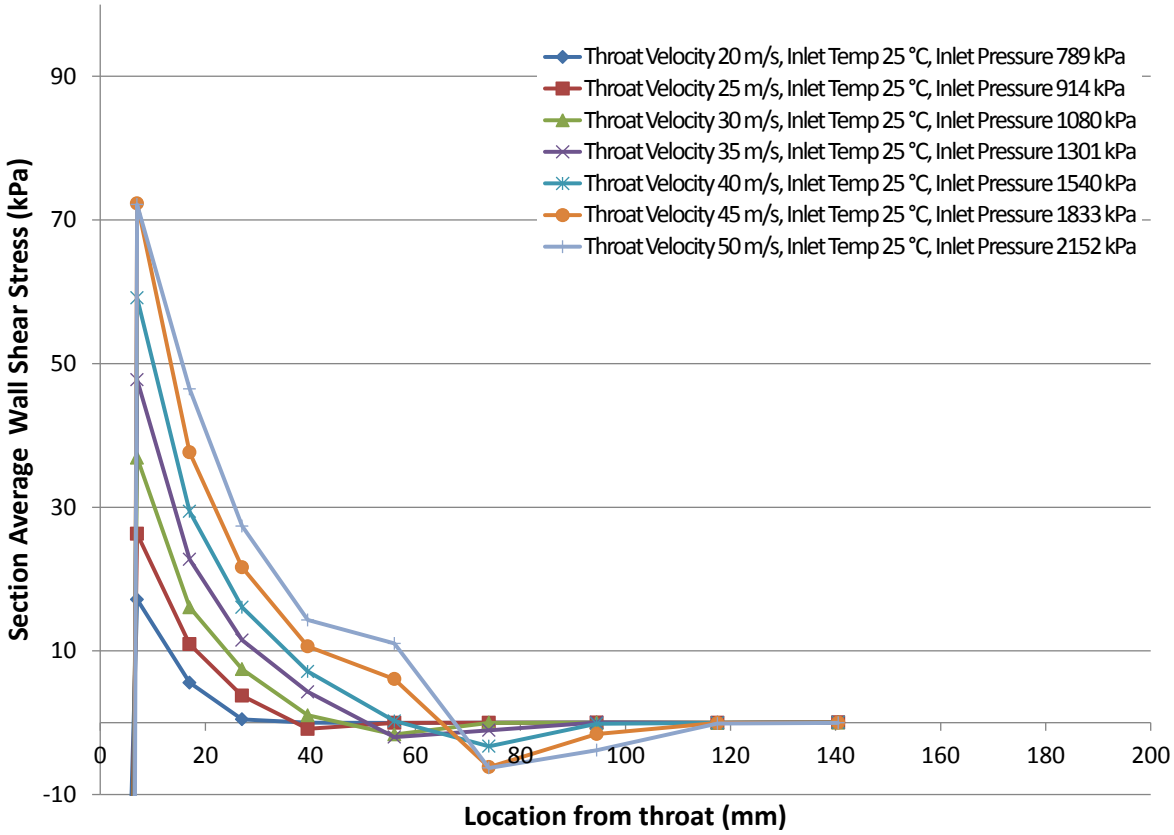

Figure 6.11: Nozzle A, Average Wall Shear Stress vs Location, $\tau > 0$

Comparing with Figure 6.5, it would seem as though shear tracks with some form of velocity, be it Mach number, mass flux, or some other flow related velocity. It appears as though negative values occur again further down the nozzle. It is unknown why the shear values further down the

nozzle are negative, though their presence in a relatively slow section would lend credence to the idea that the model is not quite adequate in handling non-equilibrium effects. The negative values also might be an artifact of uncertainties in our sensor readings. Similar behavior is seen in all nozzles with both the HEM and separated flow models.

6.3 Summary

The results of applying the models developed in Chapter 3 to our data of Chapter 4 have been presented. The model data supports the premise that our flow is sonic. Several observations have been made with regard to the flow. First, the lowest pressure does not correlate with the highest quality, but increasing throat velocity does yield higher qualities. The highest quality and mass flux does seem correlate with point at which the flow drops back to subsonic velocities. Laying out a plot of velocity vs void fraction, it appears as though the transition between sonic to subsonic velocities occurs as an increase in void fraction causes velocity to drop below the speed of sound.

Chapter 7 - Conclusion

Cavitation is an important phenomenon in fluid flow. Cavitation occurs in devices such as valves, orifices, and metering devices when local pressure of a flow drops below the saturation pressure as it moves through such a device due to the device geometry. An important subset of cavitating flow occurs when the flow becomes sonic and is able to accelerate with expanding area. Few models exist that take into account all aspects of such flows, especially for flows of variable area such as is found in a converging-diverging nozzle.

In this paper, two models, the homogeneous equilibrium model and separated flow model, were developed for cavitating flows in a converging-diverging nozzle by applying the integral form of the conservation equations of mass, momentum and energy. These models include are developed to include both friction and the variable area of a converging-diverging nozzle.

These models were then applied to data collected by the author for four nozzles of various geometries. The nozzles were tested in a custom experimental apparatus with R-134a as the fluid of interest. The data was examined both with and without applying the developed models.

Several conclusions are made regarding both the models and the data. First, the models support the conclusion that our flows are sonic. The behavior of pressures and temperatures in the nozzle is unlike what would occur were the flow not sonic. Second, the models developed likely do not accurately model all aspects of the flow, especially in what are likely non-equilibrium regions near the throat, reflected in the negative shear stresses calculated by the momentum equation. Finally, maximum void fraction occurs in the nozzles when flow decreases in velocity to a Mach number of 1, transitioning from sonic to subsonic.

Bibliography

Akagawa, K., T. Fujii, J. Ohta, K. Inoue and K. Taniguchi (1987). Study of Performance Characteristics of the Nozzles for Subcooled Hot Water. Proceedings of the 1987 ASME-JSME Thermal Engineering Joint Conference., Honolulu, HI, USA, ASME.

Brennen, C. E. (1995). Cavitation and bubble dynamics, New York: Oxford University Press.

Chern, M.-J., C.-C. Wang and C.-H. Ma (2007). "Performance test and flow visualization of ball valve." Experimental thermal and fluid science **31**(6): 505-512.

Collier, J. G. and J. R. Thome (1994). Convective Boiling and Condensation, Oxford University Press.

Elias, E. and G. S. Lellouche (1994). "Two-phase critical flow." International Journal of Multiphase Flow **20**(SUPPL. 1): 91-168.

Fox, R. W., A. T. McDonald and P. J. Pritchard (2006). Introduction to Fluid Mechanics, Wiley.

Henry, R. E. and H. K. Fauske (1971). "The Two-Phase Critical Flow of One-Component Mixtures in Nozzles, Orifices, and Short Tubes." Journal of Heat Transfer **93**(2): 179-187.

Ishii, R., Y. Umeda, S. Murata and N. Shishido (1993). "Bubbly flows through a converging–diverging nozzle." Physics of Fluids A: Fluid Dynamics (1989-1993) **5**(7): 1630-1643.

Lemmon, E., M. L. Huber and M. O. McLinden (2013). NIST Standard Reference Database 23: Reference Fluid Thermodynamic and Transport Properties - REFPROP, Version 9.1. Standard Reference Data Program. Gaithersburg, National Institute of Standards and Technology.

Levy, S. (1999). Two-Phase Flow in Complex Systems, Wiley.

Liu, J., J. Chen and Z. Chen (2008). "Critical flashing flow in convergent-divergent nozzles with initially subcooled liquid." International Journal of Thermal Sciences **47**(8): 1069-1076.

Schmidt, J. and S. Egan (2009). "Case Studies of Sizing Pressure Relief Valves for Two-Phase Flow." Chemical Engineering & Technology **32**(2): 263-272.

Schrock, V. E., E. S. Starkman and R. A. Brown (1977). "Flashing Flow of Initially Subcooled Water in Convergent–Divergent Nozzles." Journal of Heat Transfer **99**(2): 263-268.

Shin, T. S. and O. C. Jones (1993). "Nucleation and flashing in nozzles - 1. A distributed nucleation model." International Journal of Multiphase Flow **19**(6): 943-964.

Wallis, G. B. (1969). One-dimensional two-phase flow, McGraw-Hill.

Wirth, K. E. and M. Rossmeissl (2006). Critical mass-flow in orifice-nozzles at the disintegration of superheated liquids. 2006 2nd ASME Joint U.S.-European Fluids Engineering Summer Meeting, FEDSM 2006, July 17, 2006 - July 20, 2006, Miami, FL, United states, American Society of Mechanical Engineers.

Yang, L. and C.-L. Zhang (2005). "Two-fluid model of refrigerant two-phase flow through short tube orifice." International Journal of Refrigeration **28**(3): 419-427.

Yin, J. M. (1998). A Theoretical Model for Predicting Adiabatic Capillary Tube Performance: An Analysis and Improvement, Air Conditioning and Refrigeration Center, University of Illinois.

Appendix A - Nozzle Experimental Data and Dimensions

Table A.1: Nozzle A Data and Dimensions

Throat Diameter (mm)	1.5		IFM Tip	N/A	mm Upstream of Throat								
Diameter at Location (mm)	9.53	1.73	2.26	2.78	3.30	4.09	5.03	5.97	7.18	8.38	15.00	101.60	
Location from Throat (mm):	-2000	2	12	22	32	47	65	83	106	129	152	250	
Throat Velocity (m/s)	pinlet (kPa)	p2 (kPa)	p3 (kPa)	p4 (kPa)	p5 (kPa)	p6 (kPa)	p7 (kPa)	p8 (kPa)	p9 (kPa)	p10 (kPa)	p11 (kPa)	poutlet (kPa)	Mass Flow Rate (kg/s)
20.28	788.97	551.40	575.12	619.68	651.99	663.88	667.44	668.72	668.84	669.31	668.70	667.50	0.04336558
25.17	914.02	524.33	538.37	557.53	599.46	656.19	664.08	665.77	666.51	666.98	666.78	664.71	0.05388104
30.06	1080.30	500.06	514.90	525.76	544.16	610.62	659.75	662.98	663.75	664.40	664.30	662.21	0.06448662
35.05	1301.20	481.36	496.31	505.38	518.02	556.68	639.31	662.34	663.74	664.62	664.76	663.64	0.07518137
39.72	1539.84	458.34	476.63	484.55	495.81	523.28	588.61	654.37	661.19	662.39	662.44	660.68	0.08529067
45.00	1833.11	429.94	453.31	462.16	472.21	495.51	548.89	630.31	662.16	663.99	664.20	662.78	0.09682719
50.11	2152.26	415.70	430.15	441.86	451.50	471.34	513.63	582.44	656.50	660.90	661.47	660.21	0.10801224
Location from Throat (mm):	-2000	5	15	25	37.5	54	72	92.5	115.5	138.5	157.5	250	
Throat Velocity (m/s)	Tinlet (°C)	T2 (°C)	T3 (°C)	T4 (°C)	T5 (°C)	T6 (°C)	T7 (°C)	T8 (°C)	T9 (°C)	T10 (°C)	T11 (°C)	Toutlet (°C)	Inlet Density (kg/m^3)
20.28	25.24	22.35	22.51	22.99	23.32	23.35	23.41	23.46	23.45	23.45	23.33	25.11	1209.94
25.17	25.10	21.31	21.02	21.37	22.30	22.92	23.13	23.40	23.57	23.74	23.84	24.97	1211.37
30.06	24.74	20.15	19.74	19.80	20.53	22.03	22.55	23.01	23.31	23.61	23.87	24.84	1213.91
35.05	25.04	19.04	18.49	18.42	18.86	20.30	21.86	22.69	23.10	23.46	23.73	24.91	1213.78
39.72	25.09	18.15	17.41	17.26	17.54	18.87	20.93	22.46	23.11	23.65	24.13	24.76	1215.12
45.00	24.96	16.99	16.19	15.95	16.12	17.36	19.36	21.88	22.76	23.42	23.97	24.87	1217.71
50.11	24.78	15.62	14.87	14.58	14.68	15.70	17.68	20.86	22.34	23.15	23.78	24.74	1219.79

Table A.2: Nozzle B Data and Dimensions

Throat Diameter (mm)	1.5		IFM Tip	17.17	mm Upstream of Throat								
Diameter at Location (mm)	9.53	1.73	2.26	2.78	3.30	4.09	5.03	5.97	7.18	8.38	15.00	101.60	
Location from Throat (mm):	-2000	2	12	22	32	47	65	83	106	129	152	250	
Throat Velocity (m/s)	pinlet (kPa)	p2 (kPa)	p3 (kPa)	p4 (kPa)	p5 (kPa)	p6 (kPa)	p7 (kPa)	p8 (kPa)	p9 (kPa)	p10 (kPa)	p11 (kPa)	poutlet (kPa)	Mass Flow Rate (kg/s)
20.15	780.89	539.52	581.87	624.41	646.44	653.23	656.69	658.21	658.75	659.27	659.08	667.50	0.04309781
24.95	900.75	498.22	540.80	581.93	622.95	647.57	654.85	657.45	658.35	658.78	658.57	664.71	0.05339957
30.24	1091.49	470.50	505.99	536.14	580.93	623.89	648.14	653.48	654.89	655.48	655.33	662.21	0.06482608
34.98	1303.52	459.06	491.06	515.54	559.90	590.13	642.35	653.09	656.46	657.08	657.21	663.64	0.07506387
39.85	1552.66	452.46	481.63	496.21	538.86	563.07	614.73	644.47	653.95	655.00	655.30	660.68	0.08561096
44.96	1848.98	450.90	479.95	474.03	517.14	543.44	574.42	633.30	654.86	655.82	656.14	662.78	0.09672993
50.24	2179.46	448.35	479.03	448.73	461.25	529.44	554.91	613.08	651.64	656.29	657.04	660.21	0.10828325
Location from Throat (mm):	-2000	5	15	25	37.5	54	72	92.5	115.5	138.5	157.5	250	
Throat Velocity (m/s)	Tinlet (°C)	T2 (°C)	T3 (°C)	T4 (°C)	T5 (°C)	T6 (°C)	T7 (°C)	T8 (°C)	T9 (°C)	T10 (°C)	T11 (°C)	Toutlet (°C)	Inlet Density (kg/m^3)
20.15	25.07	22.43	22.54	22.92	23.09	23.16	23.24	23.31	23.33	23.36	23.28	23.84	1210.47
24.95	25.07	21.25	21.13	21.79	22.47	22.90	23.13	23.40	23.59	23.82	24.04	24.30	1211.23
30.24	24.87	19.79	19.32	19.99	21.02	22.08	22.56	23.01	23.31	23.61	23.91	24.17	1213.15
34.98	24.92	19.00	18.33	18.95	20.05	21.22	22.21	22.89	23.27	23.63	23.99	24.22	1214.27
39.85	24.92	18.30	17.43	17.85	18.87	19.85	21.44	22.49	23.01	23.43	23.80	24.15	1215.74
44.96	24.93	17.75	16.64	16.69	17.78	18.76	20.35	22.11	22.85	23.37	23.79	24.20	1217.58
50.24	24.82	17.19	15.88	15.03	16.08	17.82	19.21	21.52	22.61	23.27	23.76	24.21	1219.78

Table A.3: Nozzle C Data and Dimensions

Throat Diameter (mm)	1.5		IFM Tip	9.17	mm Upstream of Throat								
Diameter at Location (mm)	9.53	1.73	2.26	2.78	3.30	4.09	5.03	5.97	7.18	8.38	15.00	101.60	
Location from Throat (mm):	-2000	2	12	22	32	47	65	83	106	129	152	250	
Throat Velocity (m/s)	pinlet (kPa)	p2 (kPa)	p3 (kPa)	p4 (kPa)	p5 (kPa)	p6 (kPa)	p7 (kPa)	p8 (kPa)	p9 (kPa)	p10 (kPa)	p11 (kPa)	poutlet (kPa)	Mass Flow Rate (kg/s)
19.84	782.65	544.37	581.71	625.09	646.62	654.43	657.61	658.74	659.73	660.18	658.88	658.02	0.04336558
24.87	913.12	502.41	538.33	581.15	622.24	647.31	654.81	657.34	658.31	658.76	658.50	656.72	0.05388104
29.97	1091.72	481.99	512.74	546.83	588.14	628.43	649.49	655.24	657.30	657.80	657.60	655.81	0.06448662
34.95	1305.18	470.97	496.16	520.89	562.69	593.45	637.31	651.91	656.61	657.49	657.30	655.68	0.07518137
40.17	1567.95	465.45	489.00	494.53	538.76	566.49	617.51	645.97	656.82	658.11	658.00	656.32	0.08529067
45.37	1866.92	462.05	489.10	457.43	493.75	546.78	582.57	630.89	655.71	658.62	658.75	657.04	0.09682719
50.00	2162.23	459.43	489.46	451.04	429.25	497.17	550.54	620.66	654.04	658.33	658.93	657.32	0.10801224
Location from Throat (mm):	-2000	5	15	25	37.5	54	72	92.5	115.5	138.5	157.5	250	
Throat Velocity (m/s)	Tinlet (°C)	T2 (°C)	T3 (°C)	T4 (°C)	T5 (°C)	T6 (°C)	T7 (°C)	T8 (°C)	T9 (°C)	T10 (°C)	T11 (°C)	Toutlet (°C)	Inlet Density (kg/m^3)
19.84	24.94	22.33	22.48	22.84	23.04	23.09	23.19	23.29	23.36	23.44	23.47	23.94	1210.74
24.87	24.85	21.07	21.00	21.65	22.35	22.73	22.98	23.24	23.40	23.59	23.75	24.15	1212.17
29.97	24.94	20.10	19.71	20.34	21.29	22.19	22.72	23.15	23.42	23.69	23.92	24.27	1212.62
34.95	24.94	19.37	18.68	19.20	20.18	21.28	22.24	22.88	23.26	23.60	23.90	24.22	1214.23
40.17	24.99	18.65	17.73	17.98	18.97	20.07	21.59	22.62	23.17	23.61	23.98	24.28	1215.66
45.37	24.96	17.92	16.76	16.24	17.47	18.89	20.57	22.12	22.93	23.45	23.85	24.30	1217.31
50.00	24.94	17.10	15.85	14.37	14.12	16.67	19.03	21.45	22.56	23.23	23.70	24.27	1219.50

Table A.4: Nozzle D Data and Dimensions

Throat Diameter (mm)	1.5		IFM Tip	N/A	mm Upstream of Throat							
Diameter at Location (mm)	9.53	1.73	2.43	3.30	4.51	5.65	7.08	8.68	10.29	15.00	101.60	
Location from Throat (mm):	-2000	2	22	47	83	116	157	203	249	272	300	
Throat Velocity (m/s)	pinlet (kPa)	p2 (kPa)	p3 (kPa)	p4 (kPa)	p5 (kPa)	p6 (kPa)	p7 (kPa)	p8 (kPa)	p9 (kPa)	p10 (kPa)	poutlet (kPa)	Mass Flow Rate (kg/s)
20.00	790.34	540.73	582.13	655.09	663.85	664.21	665.07	665.79	665.39	665.33	663.21	0.04278939
25.01	916.17	504.64	534.00	598.39	655.24	656.96	658.29	658.71	658.90	658.69	656.70	0.05355864
30.07	1090.79	474.33	501.16	543.48	651.20	654.59	656.55	657.15	657.23	657.11	655.11	0.06446719
34.58	1287.63	454.31	478.33	511.38	633.96	653.89	656.52	657.32	657.60	657.40	655.43	0.07422661
39.91	1560.00	424.49	444.39	475.47	569.13	652.75	657.31	658.40	658.85	658.78	656.69	0.08578437
44.99	1845.60	419.44	409.42	446.03	524.47	634.48	656.38	657.80	658.41	658.32	656.30	0.09685174
49.92	2171.40	429.53	383.37	419.32	489.19	575.41	655.34	657.42	658.24	658.22	656.20	0.1075957
Location from Throat (mm):	-2000	5	25	54	88.5	123	166.5	212.5	258.5	277.5	300	
Throat Velocity (m/s)	Tinlet (°C)	T2 (°C)	T3 (°C)	T4 (°C)	T5 (°C)	T6 (°C)	T7 (°C)	T8 (°C)	T9 (°C)	T10 (°C)	Toutlet (°C)	Inlet Density (kg/m^3)
20.00	25.05	22.22	22.35	23.48	23.71	23.78	23.82	23.82	23.81	23.80	24.14	1210.96
25.01	24.93	20.67	20.25	22.03	23.08	23.49	23.68	23.83	23.97	24.03	24.24	1211.90
30.07	24.92	19.12	18.31	19.96	22.43	23.20	23.50	23.71	23.91	24.06	24.16	1213.38
34.58	24.85	17.76	16.70	18.12	21.50	22.96	23.43	23.69	23.93	24.12	24.20	1214.72
39.91	24.82	16.01	14.67	15.85	19.40	22.54	23.24	23.61	23.91	24.13	24.22	1216.46
44.99	24.86	14.34	12.74	13.92	17.22	21.86	23.01	23.55	23.89	24.15	24.22	1218.07
49.92	24.87	13.47	11.15	12.22	15.24	20.44	22.71	23.45	23.84	24.10	24.22	1219.79